Dust sources in Westernmost Asia have a different geochemical fingerprint to those in the Sahara

Tereza Kunkelova[1], Anya Crocker[1], Amy M. Jewell[1], Paul S. Breeze[2], Nick A. Drake[2], Matthew J. Cooper[1], J. Andrew Milton[1], Mark Hennen[3], Maria Shahgedanova[4], Michael Petraglia[5], Paul A. Wilson[1]

1. University of Southampton, Waterfront Campus, National Oceanography Centre, Southampton, SO14 3ZH, UK
2. Department of Geography, Bush House North East Wing, Kings College London, London, WC2B 4BG, UK
3. School of Earth and Environmental Sciences, Cardiff University, Park Place, Cardiff, CF10 3AT, UK
4. Department of Geography and Environmental Science, University of Reading, Whiteknights RG6 6AB, UK
5. Australian Research Centre for Human Evolution, Griffith University, Brisbane, Queensland, 4111, Australia

ABSTRACT

Dust is an important component of Earth's climate system, directly affecting the global radiation budget and hydrological cycle. The interaction of aerosols with clouds and its impact on regional and global energy budgets remains one of the largest sources of uncertainty in climate model predictions. Records of terrigenous dust accumulation in geological archives also provide a potentially powerful way to assess past changes in hydroclimate. Western Asia, including the Arabian Peninsula, is second only to the Saharan Desert in contributing dust to the global atmosphere. Yet, while satellite-derived maps of dust source activation frequency (DSAF) provide an increasingly granular understanding of the different dust sources within these regions today, our ability to fingerprint their windblown contributions to geological archives is rudimentary, severely limiting the use of dust-based records to reconstruct past changes in continental hydroclimate. A main limitation is a poor understanding of the mineralogical and geochemical composition of the bedrock geology and, more importantly, of the readily deflated unconsolidated sediments in these regions. Here we use published data to produce a DSAF map, centred on the Arabian Peninsula and extending from North Africa to Western Asia (~40-10 °N; ~25-65 °E), and we present new radiogenic isotope (Sr and Nd) data from unconsolidated surface sediment samples at active dust-producing sites. We combine our new Sr and Nd data with sparse data on sediments from the literature and the DSAF data to define three new preferential dust source areas (PSAs) in Westernmost Asia: (i) the central belt of the Arabian Peninsula, (ii) the Southern Levant and (iii) Mesopotamia. All three of these PSAs are geochemically distinct from Saharan dust sources. Long-range sediment transport by the Blue Nile and its tributaries, and the Tigris-Euphrates River system exerts a strong influence on the geochemical fingerprints of dust sources in the Eastern Sahara and Mesopotamia, respectively. The isotopic signature of active dust sources in the central belt of the Arabian Peninsula shows only modest correspondence to underlying bedrock geology suggesting wide scale mixing by aeolian transport internally and/or a weak imprint of palaeo humidity (e.g. localized river reactivation) on dust source composition in comparison to the Eastern Sahara. Our results provide surer foundations for fingerprinting the sources of continental dust accumulating in marine, lacustrine, speleothem and ice archives, an important step in improving our understanding of Quaternary rainfall climate in arguably the most water-stressed region on Earth.

Keywords:

Arabian Peninsula, North Africa, Southwest Asia, dust source, radiogenic isotopes, εNd, $^{87}Sr/^{86}Sr$.

1 INTRODUCTION

Mineral dust is a major contributor to atmospheric aerosol loading and plays an important role in Earth's climate system, directly and indirectly impacting atmospheric processes and terrestrial and oceanic environments. Dust affects the global radiation budget by absorbing, scattering and re-emitting solar radiation (Schepanski, 2018) and the hydrological cycle both directly, by stimulating cloud nucleation and indirectly, by influencing radiative forcing (Wurzler et al., 2000). As an airborne pollutant, dust exerts a deleterious influence on human cardiovascular and respiratory health (Khaniabadi et al., 2017; Tam et al., 2012). Long-range dust transport influences the carbon and nitrogen cycles by providing macro and micro-nutrients to marine and terrestrial ecosystems, driving marine phytoplankton growth in nutrient limited regions and promoting carbon dioxide drawdown from the atmosphere (Jickells et al., 2005; Moore et al., 2013).

Remotely sensed data sets provide the means to map dust sources and transport pathways over large geographical areas. Early work using ultraviolet, infrared and visible imagery identified the common environmental characteristics of major atmospheric dust sources around the world (Prospero et al., 2002; Ginoux et al., 2004), marked endorheic basins as dust source 'hot spots' (e.g., Washington et al., 2003) and documented long-range intercontinental transport pathways (Kaufman et al., 2005). Aerosol optical depth (AOD) data from the Total Ozone Mapping Spectrometer (TOMS), combined with output from atmospheric circulation models yield estimates of dust emission fluxes and the contributions to the total global dust load of different dust producing regions (e.g. Ginoux et al., 2004). These observations show that globally, atmospheric dust loading is dominated by a northern hemisphere 'dust belt' that extends from North Africa through the Arabian Peninsula and deep into Central Asia (Figure 1) and palaeoclimate records from the North Atlantic Ocean show that the main engine of dust production today, the Sahara, has been rhythmically arid and exporting dust for at least the last 11 million years (Crocker et al., 2022).

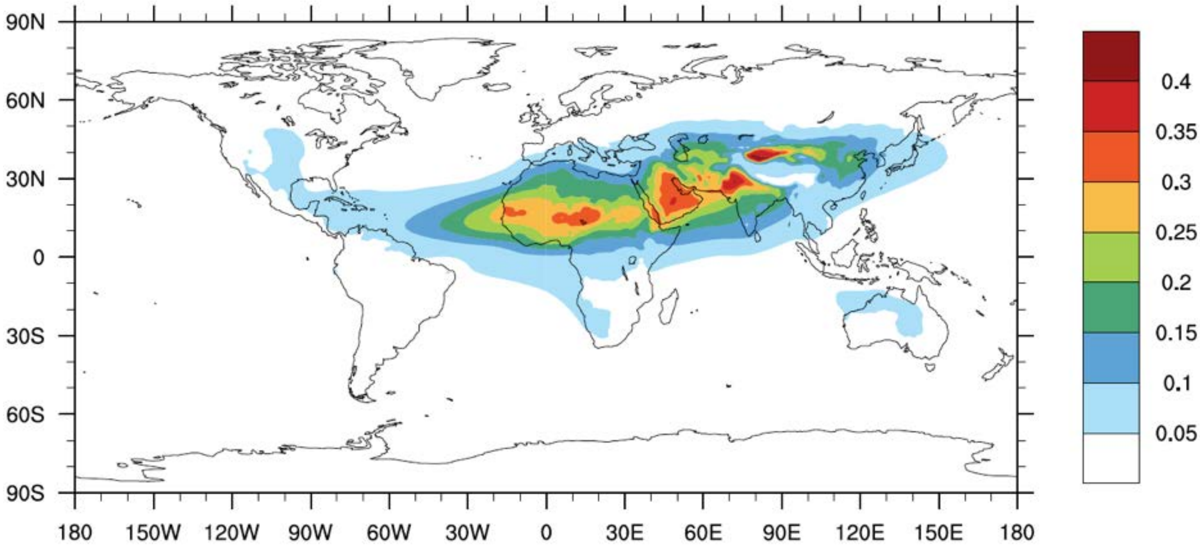

Figure 1. Global dust aerosol optical depth (AOD) averaged over the ten year period between 2003 and 2012. AOD is taken from the European Centre for Medium Range Weather Forecasts Monitoring Atmospheric Composition and Climate reanalysis data set (6-hourly resolution, 550 nm and 0.75° x 0.75° grid spacing). Legend indicates annual dust emission fluxes in g m^{-2} $year^{-1}$. Figure from Schepanski (2018).

While the overall global pattern of atmospheric dust loading in these data is clear, deflation events are triggered by events at the synoptic-, meso- and local scale and thus, poorly resolved by data sets of low temporal- and spatial- resolution because they can conflate dust emission and dust transport. To tackle this transport bias problem, Schepanski et al. (2012) pioneered the use of Meteosat Second Generation (MSG) Spinning Enhanced Visible and Infrared Imager (SEVIRI) dust index images to identify dust emission sources from images collected every 15 minutes. This method provides a way to deconvolve dust emission and dust transport and allow quantitative mapping of modern dust source activation frequency (DSAF) in North Africa (Schepanski et al., 2012 and references therein) and dust events in Western Asia, including the Arabian Peninsula (Hennen 2017).

These improvements in our knowledge of dust sources and their activation provide an important foundation to developing an improved understanding of the causes of temporal variability in the dust accumulated in marine and terrestrial paleoclimate archives (e.g., lacustrine, speleothem and ice core records) (Clemens et al., 1996; Kutuzov et al., 2019; Vaks et al., 2013). However, our ability to build on these improvements is hindered by a rudimentary capacity to fingerprint different dust sources. Thus, we lack a well-developed source-to-sink understanding of dust mobilisation and attempts to use dust-based records to reconstruct changes in past continental climate on geological timescales (e.g. Clemens et al., 1996; deMenocal, 2004) are often undermined by a persistent attribution problem (poorly constrained provenance). An improved knowledge of the mineralogical and geochemical composition of continental dust source regions is needed. This is a far from trivial undertaking given the areal coverage required and the logistical challenges of working in these field areas. Most of the early work was undertaken in North Africa (e.g. Abouchami et al., 2013; Palchan et al., 2013; Scheuvens et al., 2013; Skonieczny et al., 2013 and references therein) and East Asia (e.g. Chen et al., 2007) but it has tended to rely on data from ad hoc collections of samples and substrates many of which are not necessarily representative of the dust lofted into the atmosphere. There is now a growing awareness of the need to work on unconsolidated sediments from active dust source areas (e.g. Aarons et al., 2017; Jardine et al., 2021; Jewell et al., 2021) and, in a further step, Jewell et al., (2021) applied weightings to geochemical data for dust source activation frequency to define three preferential dust source areas (PSAs) in North Africa. However, information on the geochemistry of unconsolidated sediments from dust-producing regions in West Asia are extremely sparse and data from the Arabian Peninsula are particularly limited.

Here we present new Sr and Nd radiogenic isotope data on readily deflated unconsolidated sediments from dust-producing sites from West Asia and combine them with published data sets. We integrate the dust activation data of Schepanski et al. (2012) and Hennen (2017) to produce a composite dust source activation frequency map centred on the Arabian Peninsula extending from North Africa to Western Asia (~40-10 °N; ~25-65 °E). We then follow the approach of Jewell et al. (2021) by applying weightings to our radiogenic isotope data based upon dust source activation frequency to estimate the isotopic signature of aeolian material exported from distinct regional dust-producing areas identified across the region. Using this DSAF-weighted geochemical fingerprinting approach, we define three PSAs in Westernmost Asia: (i) the central belt of the Arabian Peninsula, (ii) the Southern Levant and (iii) Mesopotamia – all of which are isotopically distinct from the PSAs of the Sahara. We also explore the potential isotopic signature of dust from a fourth PSA, a region in eastern Iran that incorporates the Sistan and Lut deserts. Our work provides more solid foundations for geochemically fingerprinting different dust sources and their contributions to marine and terrestrial climate archives. In this way we help to develop an improved framework for deciphering changes in palaeo continental aridity and wind systems.

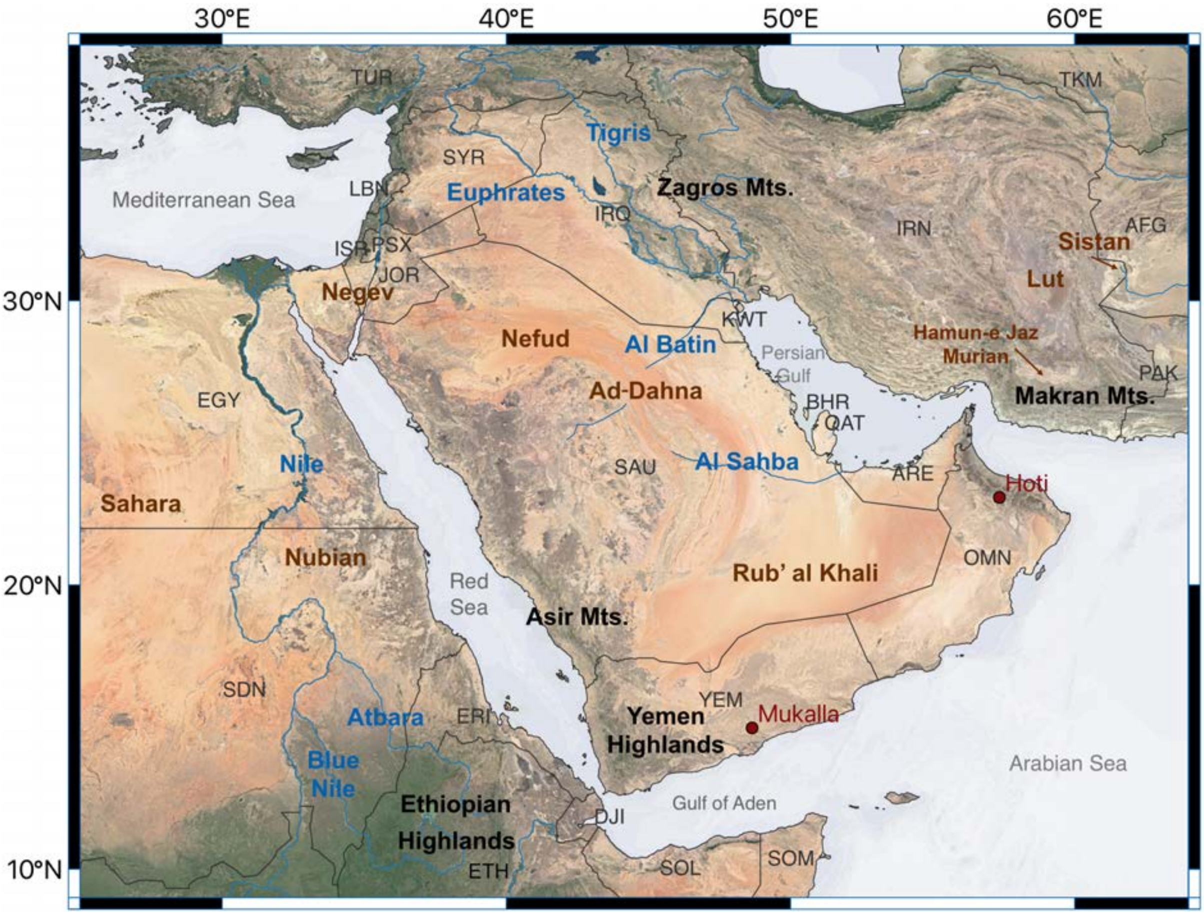

Figure 2. Study region with place names and features referred to in the text: deserts and desiccated inland lake basins labelled in brown, highland regions in black (bold), major rivers and wadis in blue, seas and gulfs in grey, caves in red. Three letter International Organisation for Standardisation (ISO) international state codes and boundaries shown in black. Base map from Google Earth.

2 STUDY REGION

2.1 Regional Climate and the Importance for Dust Generation

Dust activation is controlled by both wind strength and the availability of deflatable sediment, which is strongly influenced by hydroclimate. Strong wind gusts are an important driver of dust entrainment (McGee et al., 2010), however, in arid to semi-arid regions with fine surface soils, even relatively weak winds can induce dust storm events (Middleton, 2019). The most active sources of dust today are commonly associated with topographic lows in regions with very low annual rainfall (less than 200 – 250 mm/yr) (Middleton, 2019 and references therein).

During long periods of limited to no rainfall, soils become less cohesive and vegetation cover declines, increasing the availability of readily deflated material, although protective surface crusts can also develop and hinder deflation (Bullard et al., 2011). Consequently, unconsolidated, un-armoured and un-incised surfaces are often key to driving dust emissions on seasonal to geological timescales and dried ephemeral lake- and river- beds are particularly important as dust sources (e.g. Bakker et al., 2019; Bullard et al., 2011). The emitted dust can then be transported downwind over hundreds or even thousands of kilometres. For example, dust deposits identified in West Asia, India, the Red Sea, the eastern Mediterranean Sea and the Arabian Sea have all been suggested to be sourced from the Arabian Peninsula (Ben Israel et al., 2015; Bodenheimer et al., 2019; Hartman et al., 2020; Kumar et al., 2020; Schnetger et al., 2000; Sharifi et al., 2018; Suresh et al., 2021).

Located under the descending limb of the Hadley Cell, North Africa, the Arabian Peninsula and Southwest Asia (Figure 3) are predominantly arid. Today, the interior of the Arabian Peninsula receives less than 80 mm/year precipitation (Enzel et al., 2015) and features the Nefud Desert, the Rub' al Khali (the world's largest sand sea) and the interconnecting arid sandy terrain known as the Ad-Dahna (Figure 2). The southernmost parts of the Arabian Peninsula, such as the Yemen Highlands and Asir Mountains, receive summer monsoon-derived rainfall (Figure 3C). In the north of the region, precipitation is derived by the mid-latitude westerlies, bringing rainfall across the Southern Levant and Mesopotamia during winter months (Figure 3D) and delivering 500 to 800 mm of precipitation annually (Enzel et al., 2015).

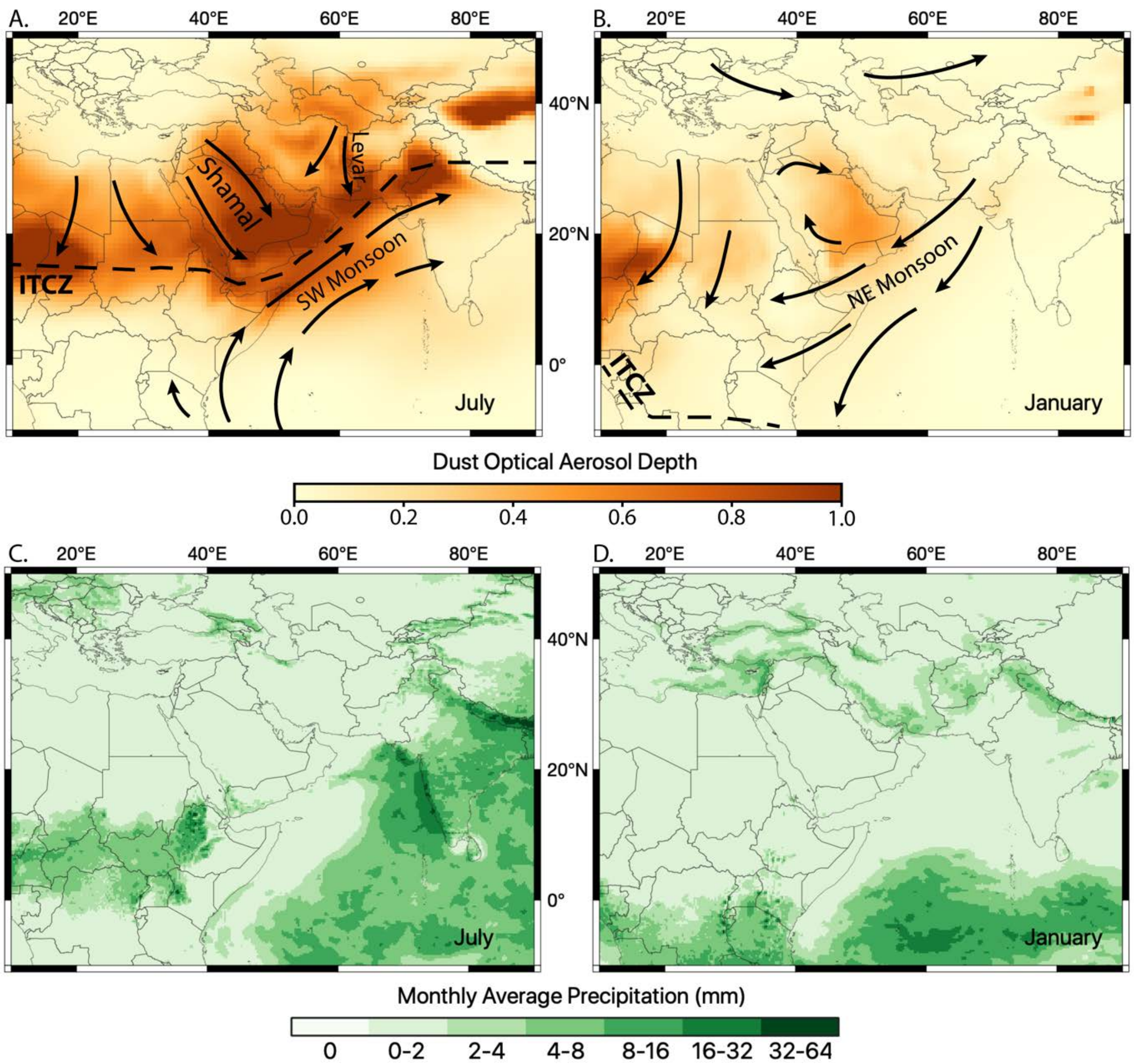

Figure 3. Top: Schematic wind patterns over Dust Aerosol Optical Thickness map at 550 nm from 2020 Copernicus Atmosphere Monitoring Service (CAMS) global Atmospheric Composition Reanalysis 4 (EAC4) for (A) boreal summer (July) and (B) boreal winter (January) (Inness et al., 2019). Darker shades indicate higher aerosol concentrations. Arrows indicate wind direction at 850 hPa, dashed line represents the intertropical convergence zone (ITCZ) (based on monthly composites from National Oceanic and Atmospheric Administration (NOAA) data accessed from the IRI Climate Data Library (iridl.ldeo.columbia.edu)). Bottom: Monthly average precipitation from 2020 using ERA5 global reanalysis dataset (in mm) for: C. July and D. January. Darker shades indicate higher precipitation (Hersbach et al., 2020). National boundaries in grey.

Wind directions and rainfall over the Northern Arabian Sea and the surrounding landmasses are distinctly seasonal (Figure 3). Atmospheric circulation over the region is modulated by the interaction of the African, Asian, and European climatic systems. The East African monsoon is connected to the larger Indo-Pacific-Asian monsoon system and provides rainfall to the southern Arabian Peninsula and northern to north-western parts of eastern Africa during boreal summer when the Intertropical Convergence Zone (ITCZ) migrates northwards from approximately 5°S to 15°N (Nicholson, 2017). It is associated with strong low-level southwesterly summer monsoon winds blowing across the Horn of Africa and the Northern Arabian Sea towards Asia (Figure 3). Dry and warm northwesterly *Shamal* and northeasterly *Levar* winds prevail in summer (Figure 3). The northwesterly *Shamal* winds are driven by the pressure gradient difference between the Eastern Mediterranean and the low-pressure belt extending from Northwest India through Pakistan and Afghanistan to Iran and they over-ride the summer southwest monsoon winds at the ITCZ (Yu et al., 2015). The northeasterly *Levar* winds are driven by the pressure differential between Central Asia and the Indo-Pakistan thermal low associated with the South Asian summer monsoon (Kaskaoutis et al., 2017). In winter, the ITCZ migrates southwards and the monsoon wind direction reverses with dry northeasterly winds blowing from the Indian subcontinent across the Arabian Peninsula, Southwest Asia, and the Horn of Africa (Figure 3). While the details are contested, palaeoclimate records from the northern Indian Ocean and numerical climate modelling experiments suggest that this regional pattern of atmospheric circulation was established during the Middle to Late Miocene (e.g. Betzler et al., 2016; Bialik et al., 2020; Clift et al., 2019; Huang et al., 2007; Kroon et al., 1991; Sarr et al., 2022; Sepulchre et al., 2006)

2.2 Quaternary palaeoclimate record of the Arabian Peninsula region

Quaternary climate reconstructions from terrestrial archives (speleothem and lacustrine deposits) on the Arabian Peninsula and across much of the Middle East show astronomically paced shifts between arid and humid conditions. Speleothem deposits from across the Middle

East can record changes in precipitation patterns and dustiness over geological timescales. Stalagmite deposits in the Negev Desert, Israel (Figure 2) reveal wet conditions at ~3.1, 1.7 and 1.25 Ma, followed by short intermittent humid intervals (Vaks et al., 2013). In Mukalla Cave, Yemen, a total of 21 pluvial events are recorded from ~1.1 Ma, with four pluvial events occurring during the last 150 ka (during marine isotope stages (MIS) 5e, 5c, 5a and 1) (Figure 2) (Fleitmann et al., 2011; Nicholson et al., 2020). These events correspond to speleothem growth recorded in the Negev Desert and Hoti cave in Northern Oman (Figure 2), suggesting that more humid conditions were widespread across the Arabian Peninsula during boreal summer insolation maxima (Fleitmann et al., 2011; Nicholson et al., 2020; Vaks et al., 2013). Further evidence for past rainfall comes from dated lacustrine deposits with humid intervals identified at around 410, 320, 200, 130-70, and 10 ka (Matter et al., 2015; Petraglia et al., 2012; Rosenberg et al., 2013, 2012, 2011; Sharifi et al., 2018). During these intervals, the landscape changed from desert to grasslands with shallow marshes and lakes providing a "window of opportunity" for early hominin dispersals into Southwest Asia (Enzel et al., 2015; Fleitmann et al., 2011; Groucutt et al., 2021; Nicholson et al., 2020; Petraglia, 2005; Roberts et al., 2018). Thus, integration of archaeological, palaeontological, and continental climate data sets provides an improving context that permist a better understand early hominin migration out of Africa.

While lacustrine deposits are generally consistent with speleothem records in identifying past humid periods the chronological frameworks for these palaeolake deposits are often poorly constrained (Rosenberg et al., 2013). Moreover, although speleothem records from the southern Arabian Peninsula reveal spectacular records of past drought conditions caused by weakening of the summer monsoon (e.g. Fleitmann et al., 2022), lake and speleothem records from the interior of the region are typically restricted to humid intervals (precipitation rates

>300 mm yr^{-1} for speleothems) and thus provide only limited information on aridity because speleothem formation, which is lithologically-dependent anyway, ceases while lakes are prone to desiccation and erosion (Vaks et al., 2013, 2010).

It has long been recognised that dust records from continuous and well-dated marine sediment archives have the potential to provide information on changes in continental aridity (e.g. Clemens et al., 1996; deMenocal, 2004) and records from the Red Sea, the Arabian Sea and eastern Mediterranean document past hydroclimate changes in the region (e.g. Ehrmann and Schmiedl, 2021; Grant et al., 2017; Hartman et al., 2020; Palchan et al., 2013; Palchan and Torfstein, 2019; Pourmand et al., 2004; Roberts et al., 2011; Torfstein et al., 2018). However, our understanding of the provenance of dust supply to these marine archives is weak and represents a first order limitation on the insight provided on past climate variability. To upgrade our ability to fingerprint regional changes in aridity and dust supply to the oceans we need to both (i) ensure that geochemical measurements of the terrigenous fraction in marine sediment archives are not overprinted by contaminating marine phases (Jewell et al., 2022) and (ii) improve our understanding of the composition of different dust sources in the region (this study).

2.3 Geology

The Arabian Plate is one of the smallest and youngest of Earth's lithospheric plates, dating to around 25 Ma when rifting in Northeast Africa formed the Gulf of Aden and the Red Sea (Stern and Johnson, 2010). The upper crust consists of three main components: (i) the Arabian-Nubian Shield, (ii) Phanerozoic sedimentary cover and (iii) Cenozoic flood basalts (Figure 4). The Arabian-Nubian Shield (ANS) is part of a thick resistant crystalline basement that formed in the Precambrian during the East African Orogeny (900–500 Ma) located along the north-south suture zone (Stern and Johnson, 2010). The ANS covers Northeast Africa and the western Arabian Peninsula and, where exposed, it forms high topographic features up to around 3100 m in elevation. Phanerozoic sedimentary cover stretches eastwards from the ANS (Figure 4), dominates central and eastern areas of the Arabian Peninsula and is of lower topographic elevation, with most areas lying below 1000 m above sea level (Stern and Johnson, 2010). Cenozoic flood basalts (called *'harrats'*) uncomformably overlie the Arabian Shield and the Phanerozoic sedimentary succession in the western and north-western parts of the Arabian Peninsula (Stern and Johnson, 2010). In the Southern Levant region, the underlying geology varies in composition from the Precambrian Arabian Shield crystalline basement to sediments and volcanic rocks of Cretaceous through Quaternary age (Figure 4). The surface geology of Mesopotamia is strongly influenced by the Tigris and Euphrates river systems (Figure 2 and Figure 4). Both rivers originate within the fault zone in Anatolia where they drain the basaltic rocks of their headwaters. In their lower reaches, as they flow southwards from Turkey into Syria and Iraq, their flood plains are made up of Neogene sediments composed of limestones, marls, sandstones, and gypsum (Figure 4).

The Lut Desert in Eastern Iran features extensive pre-Jurassic metamorphic rocks, Jurassic sedimentary rocks and Jurassic and Tertiary plutons. It also features Tertiary lava flows and pyroclastic materials (Arjmandzadeh and Santos, 2014). The Sistan Basin features the Hamoun dry lake bed, mainly composed of Quaternary silt and clay material and Holocene fluvial sand, silt and clay (Rashki et al., 2015). The Makran accretionary wedge, exposed in SE Iran and SW Pakistan, is 1000 km long and consists of Cretaceous to Miocene marine sediments, Pleistocene fluvial sandstones and siltstones and Quaternary sabkhas (Burg, 2018).

Overall, the underlying bedrock geology of Northern Africa becomes younger from west-to-east (Begg et al., 2009; Van Hinsbergen et al., 2011). The Western Saharan region is strongly influenced by the West African Craton where bedrocks are of Paleoproterozoic age while the Central Saharan region is characterized by younger basement rocks of Neoproterozoic age, and the Saharan Metacraton. The Eastern Saharan region features the Precambrian Nubian Shield but it is otherwise much younger, including post-orogenic igneous complexes, Tertiary volcanic rocks and Phanerozoic sedimentary deposits which include the Nubian sandstone formation, unconsolidated clays, and silts as well as aeolian sands, fluvial deposits and gravel (Figure 4). The Nile River flood plain in Sudan contains material derived from upstream regions originating from the Blue Nile and Atbara rivers (Padoan et al., 2011). These rivers drain the basalts of the Ethiopian Highlands that formed between the Miocene and the Pliocene (Figure 4). Eastern Sudan also features volcanic rocks (basaltic and andesitic composition) and, to a lesser extent, a variety of metamorphic rocks (mainly schists, gneisses and quartzites) overlying the Nubian Shield (Figure 4).

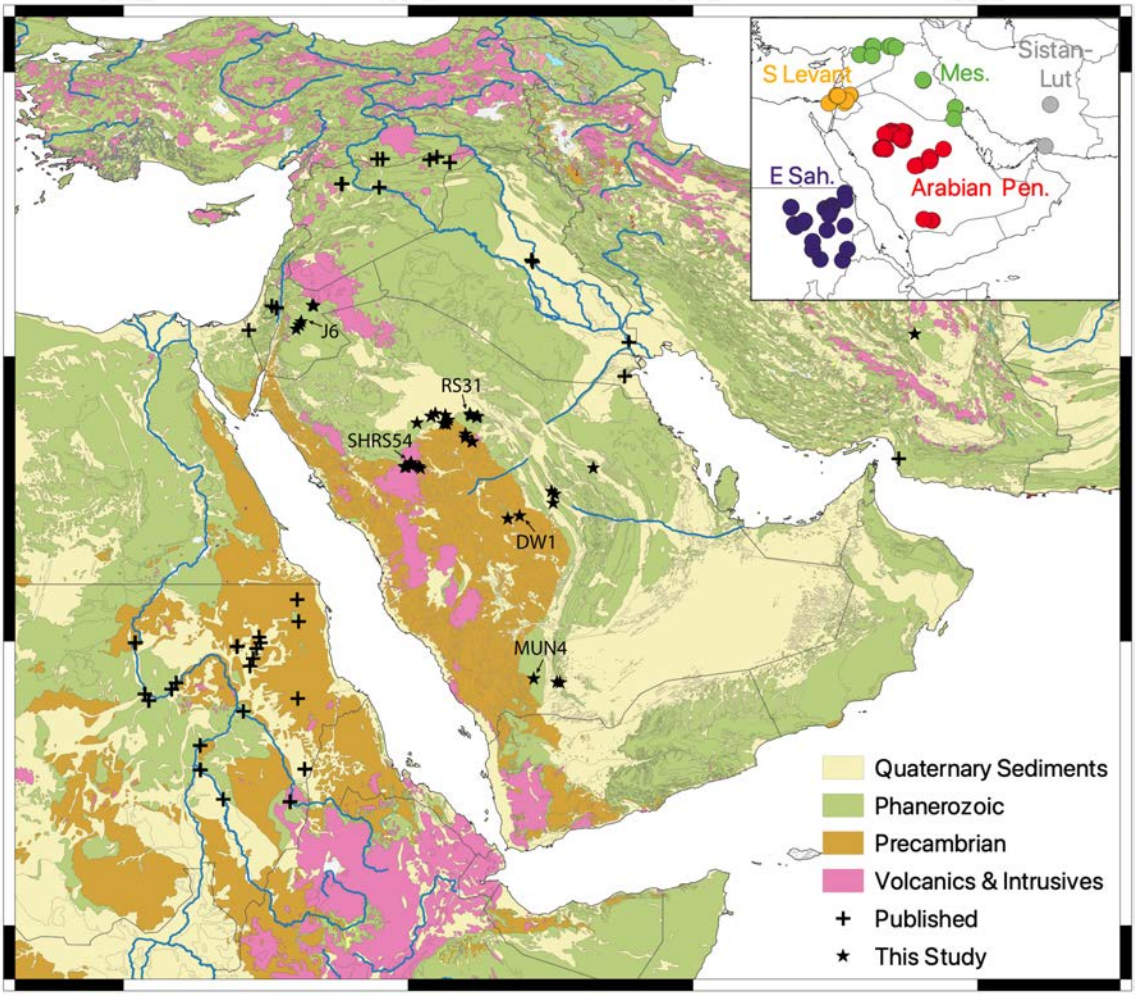

Figure 4. Simplified regional surface geology of the study region. Volcanic and intrusive rocks are shown in pink, Precambrian Arabian-Nubian Shield in brown, Phanerozoic sedimentary cover in green and Quaternary sediments in yellow.. Note the commonalities between Northeast Africa and the Arabian Peninsula (adapted from: Pawlewicz et al., 2002; Persits et al., 1997, 1999; Pollastro et al., 1997, 1999). Stars (this study) and crosses (previous work) show locations where unconsolidated sediments from active dust-producing sites were sampled for geochemical analysis (see supplementary tables 2 and 3 for details). Labelled samples (J6, SHRS54, RS31, DW1 and MUN4) are discussed in more detail in section 4.2.2. Major rivers and wadis are shown in blue. Inset shows locations of sediment samples (published and this study), coloured by their respective PSA: central belt of the Arabian Peninsula (Arabian Pen., red), Southern Levant (S Levant, yellow), Mesopotamia (Mes., green), Easten Sahara (E Sah., purple) and Sistan-Lut Desert (Sistan-Lut, grey).

2.4 Sample Descriptions

Our sampling targeted substrates and regions associated with high dust production, guided by our DSAF maps. We analysed 46 samples from several areas of the Kingdom of Saudi Arabia – the Nefud and Shuwaymis (Ha'il and Al Madinah provinces), Mundafan (Najran province), Dawadmi and Rawdat Tinhath (Riyadh province), and from Southern Jordan and the Lut Desert, Iran (Figures 2 and 4; Supplementary Table 2). Most of these samples come from desiccated lakes (n=32 samples) and riverbeds (n=9). Also included were samples from palaeosoils and fluvial wash surfaces (n=3), listed as 'other' in Supplementary Table 2. Volcanic rock samples (n=2) of a basaltic flow and a lava tube were also analysed from the Cenozoic volcanic field located within the Ha'il Province.

3 METHODS

3.1 Dust activation frequency mapping of Eastern Sahara and Westernmost Asia

We produced a regional map of dust activation frequency by integrating published data for North Africa (Schepanski et al., 2012), Southwest Asia and the Arabian Peninsula (Hennen, 2017) that were developed using high-resolution satellite observations from Meteosat Second Generation (MSG) Spinning Enhanced Visible and Infrared Imager (SEVIRI) instrument (Figure 5). Those studies used ultra-violet (UV), near-UV (deep blue) and infra-red (IR) wavelengths to separate dust from underlying terrain. Detected dust storms were then investigated and the dust traced to its source and the source location documented.

In his study, Hennen (2017) reports the total number of dust events occurring over an eight-year interval (2006-2013) (all observed events per day per 0.1° x 0.1° grid cell) while Schepanski et al. (2012) used a study interval spanning between March 2006 and February 2010 and report dust source activation frequencies (DSAF) with a maximum frequency of one dust event per day per 1° x 1° grid cell. Therefore, to integrate the two datasets, we only count a maximum of one activation event per day per 1° x 1° grid cell from the dataset of Hennen (2017), discounting additional dust events if more than one occurred in a day within the 1° x 1° grid cell. All data are presented as DSAF (in %) values following the method of Schepanski et al. (2012), and are calculated by the equation:

$$DSAF\ (\%) = (N_s/N_D) \times 100$$

$$N_s = total\ number\ of\ days\ containing\ one\ or\ more\ dust\ events$$
$$in\ 1°\ x\ 1°\ grid\ cell\ within\ a\ given\ month,$$
$$N_D = number\ of\ days\ of\ available\ satellite\ observation\ in\ the\ same\ month$$

The data used to produce our combined DSAF map of North Africa and Southwest Asia covers the interval from March 2006 to February 2010 (Supplementary Table 1). Our maps of annual and seasonal DSAFs are shown in Figures 5 and 6, respectively. Seasonal DSAFs were defined as follows i) spring (March 1 to May 31), ii) summer (June 1 to August 31), iii) autumn (September 1 to November 30) and iv) winter (December 1 to February 28/29) (Supplementary Table 1).

3.2 Radiogenic isotope analysis

Sr and Nd radiogenic isotope compositions of lithogenic material were determined on 41 unconsolidated surface sediment samples (mostly sourced from dried river and lake beds) and 2 samples of volcanic bedrock (Supplementary Table 2). All sediment samples were dry sieved to isolate the less than 32 μm fraction, except for three coarse grained samples for which we analysed bulk sediment (see Supplementary Table 2). Five sediment samples were also split into five narrower size fractions (63-45 µm, 45-32 µm, 32-15 µm, 15-4 µm and <4 µm) to investigate the influence of grain size on Sr and Nd isotope composition. Dry sieving was used to isolate grain size fractions larger than 32 µm and a two-step centrifugation method (see Bayon et al., 2015 for details) was used to separate samples at 32-15 µm, 15-4 µm and <4 µm grain size fraction. Volcanic samples were first ground to a fine powder and then analysed following the same method. Calcium carbonate was removed from all samples by adding excess 10% (v/v) acetic acid and shaking overnight (Bayon et al., 2002). Samples were then rinsed in Milli-Q water three times. From each carbonate-free sample, approximately 10 mg of sediment was digested overnight in HF-HNO_3-$HClO_4$ mixture at 130°C.

Chromatographic column separations were carried out in a clean chemistry laboratory at the University of Southampton's Waterfront Campus, NOCS. Sr and Nd were separated using cation columns (Bio-Rad AG-50W-X8 resin). The Nd fraction was then extracted by a reverse phase column (Ln-spec resin) (Bayon et al., 2002). The total column Nd blanks were negligible (10 pg and 18 pg) compared to the 200 ng Nd used for analysis of samples. Nd isotope data were analysed by multi-collector inductively coupled plasma mass spectrometry (MC-ICP-MS, Thermo Scientific Neptune). Adjustment to a $^{146}Nd/^{144}Nd$ ratio of 0.7219 and a secondary normalisation to $^{142}Nd/^{144}Nd$ = 1.141876 was used to obtain corrected Nd isotopic compositions (Vance and Thirlwall, 2002), which were then converted to ε_{Nd} notation (Jacobsen and Wasserburg, 1980) using the standard formula:

$$\varepsilon_{Nd} = \left[\frac{{}^{143}Nd / {}^{144}Nd_{sample}}{{}^{143}Nd / {}^{144}Nd_{CHUR}} - 1\right] \times 10^4$$

After the initial cation column separation, Sr was isolated using Sr-spec resin, dried down and loaded onto an outgassed tantalum (Ta) filament with 1 µl of Ta activator solution and 1.5 µl of HCl (Bayon et al., 2002). The total column Sr blanks were insignificant (38 pg and 6 pg) compared to the 1 µg Sr used for analysis of samples. Analysis was conducted using a ThermoScientific Triton Thermal Ionisation Mass Spectrometer using a multi-dynamic procedure and ^{88}Sr beam of 2 V. Exponential correction normalised to $^{86}Sr/^{88}Sr = 0.1194$ was used to correct for fractionation. NIST987 (Yobregat et al., 2017) was run as a standard in each turret yielding a mean of 0.710244 ± 0.000006 (2SD) over 22 analyses during the course of this work. The long-term average for NIST987 on this instrument is 0.710243 ± 0.000020 (2SD) over 464 analyses.

3.3 Compilation of published surface sediment radiogenic isotope data

We compiled published radiogenic isotope values of surface sediments from across our study region. Our compilation includes a range of substrates and grain size fractions ranging from <4 µm to bulk sediment (see Table 3 in Supplementary Materials) reflecting the paucity of published data from the region. We focused on data from decarbonated samples so that our results can be compared with data from marine sediments, where removal of biogenic carbonate is necessary to isolate the lithogenic fraction from marine carbonate (Jewell et al., 2022). Various protocols were used to generate the published data that we compiled (see original references). In most cases methods followed similar procedures to the ones that we used on our samples. An exception is the case of the data from Henderson et al. (2020) where bulk samples were digested for analysis without carbonate removal. From that study, therefore, we included data from fine-grained Quaternary fluvial sands but excluded data from coarser-grained Neogene sediments with anomalously unradiogenic ε_{Nd} compositions (between -13.1

and -11.4) and highly variable $^{87}Sr/^{86}Sr$ (0.70778 to 0.71037). The data compiled are available in Supplementary Table 3. The influence of grain size on dust source composition on our new data set is evaluated in section 0.

Our compilation of isotope data from the Southern Levant region includes samples of sand, Terra Rosa (reddish soil occurring in the Mediterranean climates) and valley loess surface soils (Supplementary Table 3; Haliva-Cohen et al., 2012; Palchan et al., 2018a). Note that low $^{87}Sr/^{86}Sr$ values of sediment deposits (on average 0.7094) are also reported from the Southern Levant region (Supplementary Table 3; Henderson et al., 2020; Palchan et al., 2018a), but those data come from dust inactive areas (DSAF % = 0) so do not influence our calculated PSA values.

Published data from the Mesopotamian region include samples from Iraq, Kuwait, and Syria (Supplementary Table 3; Henderson et al., 2020; Kibaroğlu et al., 2017; Kumar et al., 2020; Sharifi et al., 2018). In the southern part of the Mesopotamian region, published data include soil samples from the Abu Zirig Wetland (Iraq) and sediment samples from Baghdad and flat lands located northwest of Kuwait City, representing the Tigris-Euphrates floodplains (Supplementary Table 3). In Northern Mesopotamia, samples of fine clay and fine sands from the Euphrates floodplain show isotope values consistent with those from Southern Mesopotamia (Supplementary Table 3). Sediments along the modern Euphrates channel and its palaeo-channel originate from the Eastern Anatolian Plateau, which consists of Neogene basalts (Pawlewicz et al., 2002).

Data from active dust producing sites in Iran are particularly sparse. We know of only a single published sample from the coastal plain where many wadis drain the Makran region (Kumar et al., 2020).

3.4 DSAF-weighted isotope fingerprints for our PSAs

Isotope signatures for PSAs are commonly defined using the average and/or range of all available data within a specified region. That method provides a reasonable first order approach but gives equal weighting to all substrate isotope compositions regardless of their relative contribution to the total atmospheric dust load. To obtain more representative isotope compositions, we followed Jewell et al. (2021) in applying a dust source activity weighting to individual data points before calculating mean isotopic compositions for our PSAs. We used the 1° x 1° grid cell DSAF map shown in Figure 5. Where more than one sample was available within a single 1° x 1° grid cell, the mean isotopic composition of those samples was used. The weighted means were calculated as follows:

$$\bar{x}_{PSA} = \frac{\sum(x_i \times w_i)}{\sum w_i}$$

x_i = individual/mean sample isotope signature, w_i = DSAF

The weighted mean standard deviation for each PSA is given by:

$$st.dev_{PSA} = \sqrt{\frac{\sum (w_i \, (x_i \times \bar{x}_{PSA}{}^2))}{\frac{(N-1)\sqrt{w_i}}{N}}}$$

x_i = sample isotope signature, w_i = DSAF, N = number of samples

Thus, our approach reduces aliasing by excluding data from non-dust producing regions and is sensitive to spatial variability in DSAF between the geochemical datapoints.

4 RESULTS AND DISCUSSION

On geological timescales, mineral dust accumulated in marine and terrestrial climate archives provides a way to reconstruct long, continuous, well-dated proxy records of changing continental aridity and wind strength (e.g. Clemens et al., 1996; Crocker et al., 2022; deMenocal, 2004; Skonieczny et al., 2019; Tiedemann et al., 1994). However, to unlock the full potential of these archives, we must determine dust provenance. This is a far from straightforward task, particularly in the northern Arabian Sea where wind directions change dramatically by season with the potential to bring dust from different sources on the encircling arid and semi-arid landmasses (Figure 3). Radiogenic isotope signatures (e.g., Sr and Nd) of lithogenic material provide a powerful way to address this problem. But first, we must improve our knowledge of the isotopic composition of dust sources (Jewell et al., 2021; Scheuvens et al., 2013). Once the dust sources are identified and fingerprinted, this knowledge can be coupled to an understanding of both the seasonality of dust generation in the source region(s) and the relevant transport pathways between source and sink to provide a much more powerful and holistic understanding of past climate variability (e.g. Crocker et al., 2022).

4.1 Four main dust producing regions and the causes and seasonality of their activation

East of ~25 °E, our composite DSAF map shows four main geographically extensive regions of dust generation: (i) the Eastern Sahara, (ii) the central belt of the Arabian Peninsula, (iii)

Mesopotamia, (iv) the Sistan-Lut Desert region in eastern Iran and a fifth geographically less extensive region in the Southern Levant, which borders the Mesopotamian dust source region (Figures 4 and 5) but lies west of the watershed that defines the Tigris-Euphrates River catchment as shown by the surface hydrology in Figure 5b.

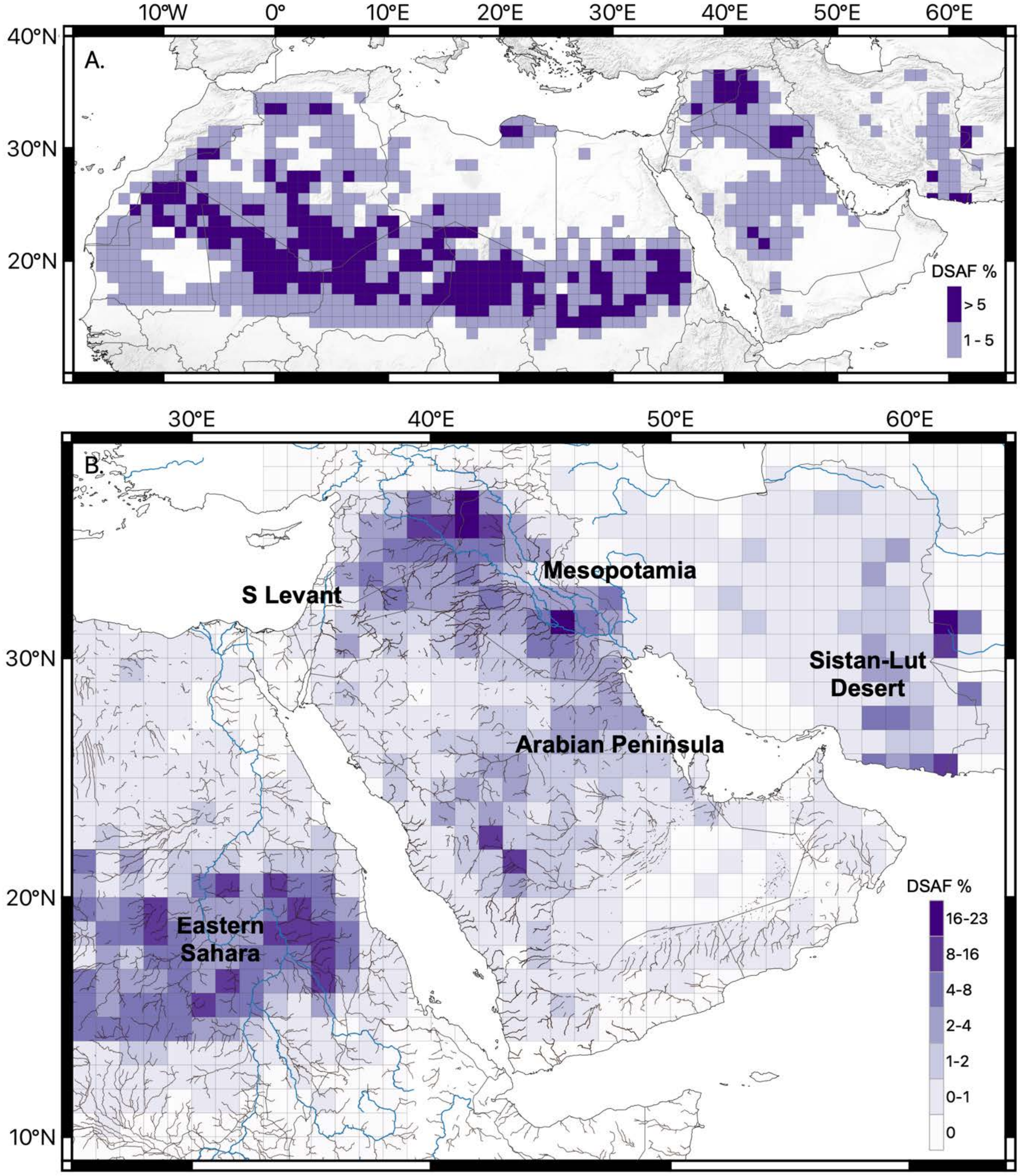

Figure 5. Annual dust source activation frequency (DSAF) map: A. North Africa and Westernmost Asia and B. Eastern Sahara and Westernmost Asia from March 2006 and February 2010 (Hennen, 2017; Schepanski et al., 2012) overlain with active river channels (blue) and palaeoriver reconstruction (brown) (Breeze et al., 2015). Intensity of coloured pixels indicates DSAF % with higher DSAF % values in darker shades (note different scales between panels A. and B.). Labels in panel B. indicate the main PSAs introduced in Figure 4B.

The highest DSAFs in the modern-day Eastern Sahara are found in the Nubian Desert in central Sudan between about 14° and 22°N (Figure 5). Seasonal DSAF maps reveal that the Eastern Sahara PSA is active all year-round with the lowest DSAF % occurring in summer (Figure 6). The most active sources of deflatable dust in this region are alluvial deposits within the Nubian Desert (Bakker et al., 2019) that formed during past intervals of higher net-precipitation, most recently the mid-Holocene African Humid Period (Tierney et al., 2011). Dust from this region is deflated and transported by the north-easterly winds that are active all year and by meso- to micro-scale winds such as haboobs, dust events that form when cold air outflows from deep convective clouds (Figure 6D). The region is estimated to produce approximately 7.5 % of the total of the North African wintertime dust (Bakker et al., 2019).

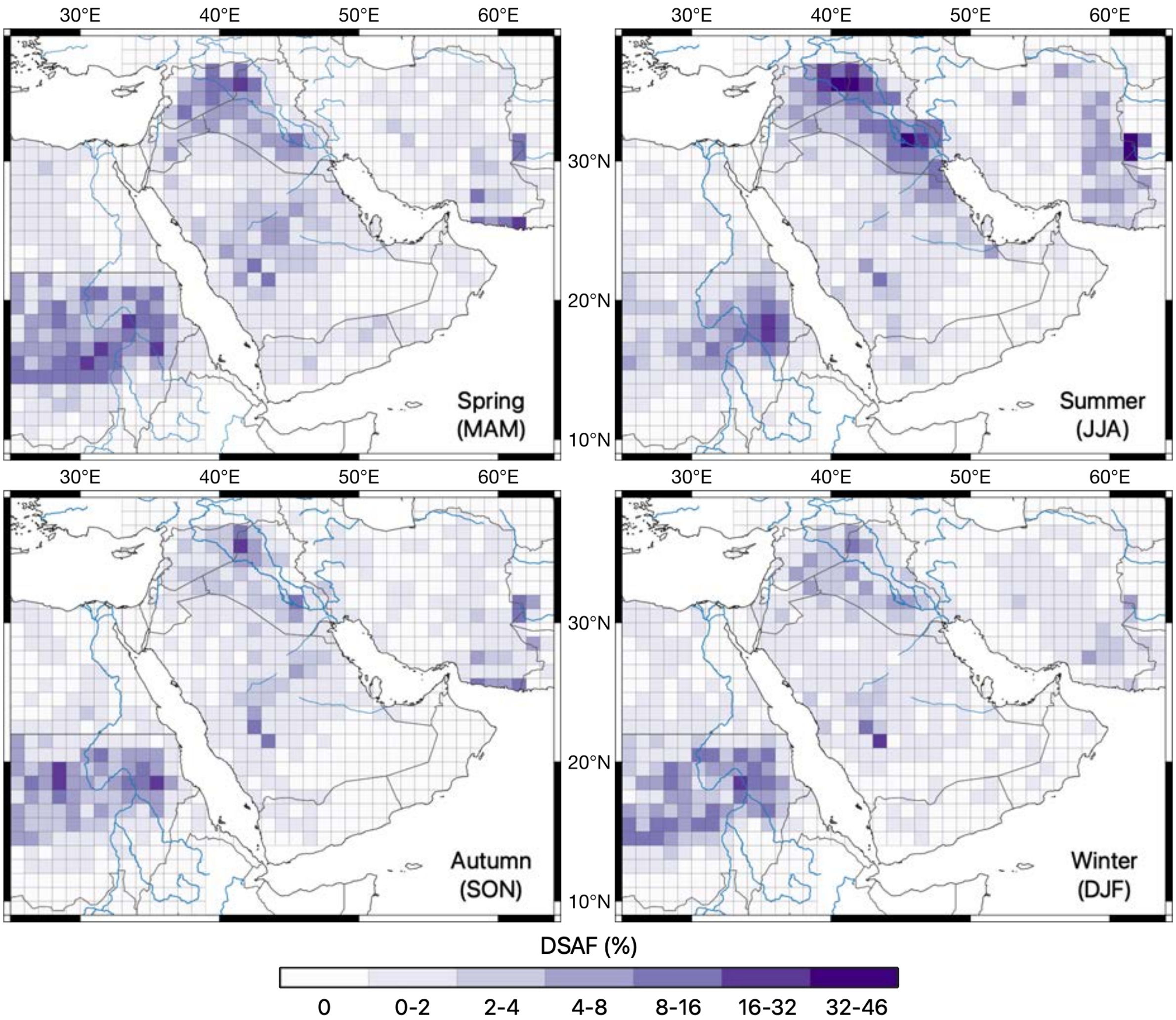

Figure 6. Seasonal DSAF (%, darker shades indicate higher DSAF): A. Spring (March 1-May 31), B. Summer (June 1-August 31), C. Autumn (September 1-November 30) and D. Winter (December 1-February 29) calculated from the recorded years between 2006 and 2010. Dust activity intensifies in Mesopotamia in spring and peaks in summer when it becomes the most active area within the study region, with lower activities in autumn and winter. The central belt of the Arabian Peninsula is most active from spring to autumn, while Eastern Sahara remains active throughout the year with highest DSAF in the winter. The Sistan-Lut Desert region of Iran is most active in summer. National boundaries in grey and major active rivers and wadis in blue.

Extensive dust-producing regions with high annual DSAFs are also observed in westernmost Asia, notably on the Arabian Peninsula, in Mesopotamia and in eastern Iran (Figure 5). Our combined regional DSAF map reveals that the highest annual DSAFs across the study area are reported in northern Mesopotamia (22.5 %), which exceeds peak DSAF in the Eastern Sahara

(15.1 %). The Mesopotamian region of high dust generation includes the entire drainage basin of the Euphrates and Tigris rivers and their tributaries (Figure 5) and is bounded by the Zagros Belt to the east. This region is most active in summer and least active in autumn (Figure 6), whereas the Eastern Sahara is least active in summer and most active in winter. Dust from Mesopotamia originates from fine alluvial sediments of the Tigris and Euphrates river basins and local sabkhas (salt flats) together with anthropogenically generated dust from agricultural practises, particularly in Syria (Ginoux et al., 2012; Hennen, 2017). High summer DSAF zones are identified in Northern and Southern Mesopotamia, with summer DSAF peaking at 45.9 % compared to 19.0 % in Eastern Sahara (Figure 6B). Our DSAF maps also show elevated dust activity (peaking in spring) in the Southern Levant, where most dust activity occurs in a region close to, but outside of, our Mesopotamian region as defined by the Tigris-Euphrates River basin, and most dust activity here occurs between spring and autumn.

The highest dust activation frequencies in the central belt of the Arabian Peninsula are concentrated in a band with a roughly northeast-southwest direction, extending from the Persian Gulf to the Asir Mountains. This region is most active in spring through autumn (Figure 6A-C) and least active in winter. Evidence of palaeorivers and palaeolake basins (which have also been interpreted as shallow marshes) is widespread across the Arabian Peninsula (Breeze et al., 2015; Enzel et al., 2015). These features play an important role in dust generation, with the Al Batin and Al Sahba wadis (Figure 2) among the major sources of dust (Ginoux et al., 2012; Hennen, 2017). In contrast, very low DSAFs are recorded in the world's largest sand sea (the Rub' al Khali), emphasising that it is the availability of finer-grained sediments, especially from the beds of ephemeral and palaeo river and lake systems, that drive deflation (Figures 2 and 5).

The Sistan-Lut Desert region, located in southern and eastern Iran, is a further prominent geographically extensive dust source region (Figure 5). This region is most active in summer (with seasonal DSAF as high as 41.3 %) and least active in winter (Figure 6B and D). The major dust-producing areas within this region are the ephemeral lakes (Lake Hammoun) in the Sistan Basin (Figure 2) (Rashki et al., 2015). High DSAFs within the Sistan-Lut Desert region also occur in the Lut Desert, the southern coast near the Makran Mountains and areas with large saline lakes (e.g. Hamun-e Jaz Murian) (Figure 2) (Gherboudj et al., 2017; Ginoux et al., 2012).

4.2 Geochemical signature of dust sources

4.2.1 Isotopic signatures of four PSAs

Our data show that dust sources in Westernmost Asia are isotopically distinct from those of North Africa (Figure 7). The Western and Central Sahara PSAs are more radiogenic in Sr and more unradiogenic in Nd than the PSAs of Western Asia while the Eastern Saharan PSA is readily distinguished from the PSAs of Western Asia (including the Arabian Peninsula) by its distinctly non-radiogenic Sr isotope composition and typically more radiogenic Nd isotope composition (Figure 7). In some ways, the offset between the West Asian and Eastern Saharan PSAs is an unexpected result because there are strong commonalities in geology between the Eastern Sahara and Arabian Peninsula, particularly around the Red Sea in the form of the Arabian Nubian Shield (Figure 4). We attribute this isotopic offset in part to overprinting by long-range fluvial transportation of sediments in the Eastern Sahara. Here, the Nile River acts as a powerful mechanism to transport lithogenic material over long distances, supplying sediment with very distinctive isotopic signatures. The Blue Nile and Atbara rivers drain the Ethiopian Highlands, contributing material to the Eastern Sahara with a radiogenic Nd (ε_{Nd} ≈

0) isotopic signature. The White Nile drains the Central African craton, which has a much more unradiogenic Nd isotopic signature ($\varepsilon_{Nd} \approx -30$) but it was responsible for less than 10% of the sedimentary load to the mid- and lower Nile prior to the construction of the Aswan Dam (Bastian et al., 2021; Padoan et al., 2011 and references therein). We see strong evidence of sediment transport by the Blue Nile and Atbara river system influencing dust source signatures in the Eastern Sahara, with samples taken along the Nile flood plains downstream of the Ethiopian Highlands showing particularly radiogenic Nd isotopic signatures (Fig 8B).

East of the Nile River, nine sites in Sudan overlying the Precambrian Arabian-Nubian Shield also show Sr and Nd isotopic signatures (0.70514 to 0.70746 and -4.1 to -1.6 for $^{87}Sr/^{86}Sr$ and ε_{Nd}, respectively, Jewell et al., 2021) that are distinct from both the reported regional intrusive and extrusive rocks from within the Nubian Shield in Northeast Sudan (0.7019 to 0.7030 and 5.1-7.7, Stern and Kroner, 1993) and the shield data compiled by Palchan et al., (2013) (0.708-0.730 and -2.5 to -0.5). This observation suggests control by sediment supply down local palaeoriver channels draining basic volcanic rock sources (see for example the work of Kröner et al., (1991) in the Red Sea Hills. In contrast, the isotopically distinctive ($^{87}Sr/^{86}Sr$ = 0.702-0.704; ε_{Nd} = 3 to 7, this study, Altherr et al., 2019 and references therein) Cenozoic flood basalts or '*harrats*' that overlie the Arabian Shield appear to exert little control on the Arabian dust sources there because our data from the palaeo-lacustrine sediments sampled from the harrats of the Shuwaymis region show very different compositions (0.71051-0.71368, $^{87}Sr/^{86}Sr$; -10.1 to -4.2 ε_{Nd}, Figure 9). This observation suggests that the palaeoriver channels that fed these ancient water bodies were reactivated less recently or extensively than the ones sampled in the Eastern Sahara.

Our calculated DSAF-weighted mean isotopic compositions for the central belt of the Arabian Peninsula (0.7115 ± 0.0012 and -6.4 ± 1.8 for $^{87}Sr/^{86}Sr$ and ε_{Nd}, respectively) and the Southern Levant (0.7116 ± 0.0011 and -6.8 ± 0.7) are isotopically indistinguishable from one another (Figure 7). These two PSA values also show good agreement with samples of dust deposited in Jerusalem (0.71225 and -6.8 to -7.2 for $^{87}Sr/^{86}Sr$ and ε_{Nd}, respectively, Palchan et al. (2018b)), aerosols collected in Eilat (-9.9 to -6.7 in ε_{Nd}, Hartman et al. (2020)) and dust suggested to originate from the Arabian Peninsula collected in Goa, India (0.71253 to 0.72909 for $^{87}Sr/^{86}Sr$ and -7.8 to -7.3 ε_{Nd}, Kumar et al. (2020) and -6.6 in ε_{Nd}, Hartman et al. (2020)) (Figure 7). Within the Arabian PSA, we find no strong isotopic distinction between sediments overlying shield- versus non-shield bedrock (Figure 8). This lack of spatial heterogeneity suggests that the dust sources of the Arabian Peninsula and Southern Levant are influenced by the homogenizing effects of aeolian mixing probably through a combination of the recycling of ancient sand deposits as reported from the Sahara (Pastore et al., 2021) and longer range transport of finer grained desiccated palaeolake and river-bed deposits as documented in the Mojave Desert (e.g. Jardine et al., 2021; Reynolds et al., 2006).

PSA	**$^{87}Sr/^{86}Sr$**	**1 sd**	**ε_{Nd}**	**1 sd**
Arabian Peninsula	0.7115	0.0012	-6.4	1.8
Southern Levant	0.7116	0.0011	-6.8	0.7
Eastern Sahara	0.7059	0.0017	-1.1	2.7
Mesopotamia	0.7087	0.0017	-3.5	1.8
Sistan-Lut Desert	0.7098	0.0005	-7.6	0.7

Table 1. Weighted mean isotopic signature with 1 weighted mean standard deviation of the Eastern Sahara (Jewell et al., 2021), the central belt of the Arabian Peninsula (Arabian Peninsula), Southern Levant, Mesopotamia and Sistan-Lut Desert PSAs (see Figure 8 for spatial definition), defined using new and published data of unconsolidated sediments. For more detail on data and references used see Supplementary Tables 2 and 3.

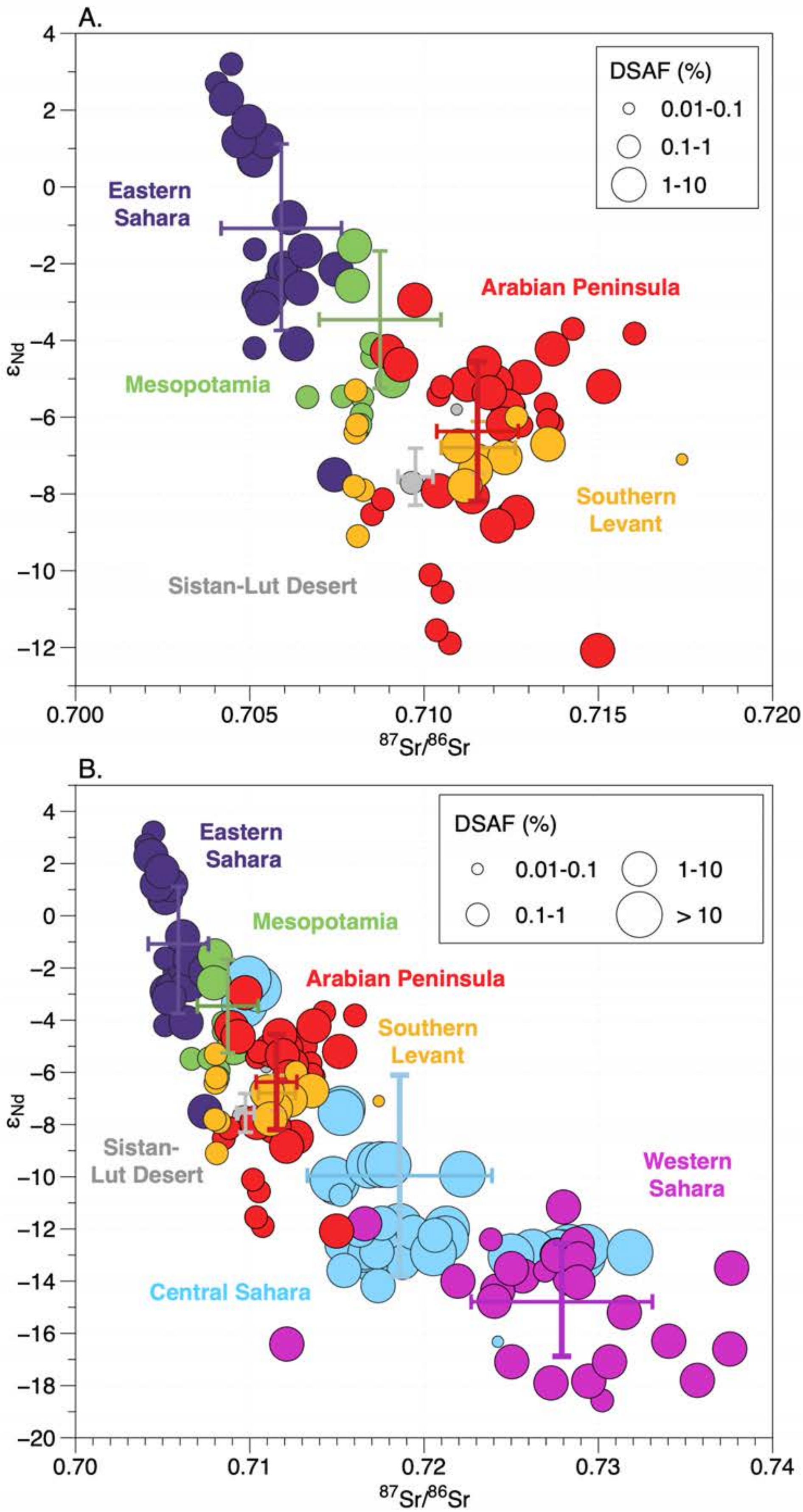
A.
DSAF (%)
0.01-0.1
0.1-1
1-10
Eastern Sahara
Mesopotamia
Arabian Peninsula
Southern Levant
Sistan-Lut Desert
εNd
87Sr/86Sr
B.
DSAF (%)
0.01-0.1
0.1-1
1-10
> 10
Eastern Sahara
Mesopotamia
Arabian Peninsula
Southern Levant
Sistan-Lut Desert
Western Sahara
Central Sahara
εNd
87Sr/86Sr

Figure 7. Sr and Nd isotopic composition of the preferential dust source areas (PSAs) in westernmost Asia and northeast Africa (A.) as defined in Figures 4 and 5B. Data shown are measurements of unconsolidated sediments from the central belt of the Arabian Peninsula (Arabian Peninsula, red) (this study), the Southern Levant (yellow, this study and Haliva-Cohen et al., 2012; Palchan et al., 2018),, Mesopotamia (green, Henderson et al., 2020; Kibaroğlu et al., 2017; Kumar et al., 2020; Sharifi et al., 2018)), Eastern Sahara (purple, Jewell et al., 2021; Padoan et al., 2011) and Sistan-Lut Desert (grey, this study and Kumar et al., 2020). See Supplementary Table 3 for further details of data used. Symbol size corresponds to the annual DSAF of the locality sampled (see Figure 8). Mean isotopic compositions weighted for DSAF with standard deviation bars are plotted for each PSA. Lower panel (B.) shows the same data as panel A compared to the western and central Sahara PSAs from Jewell et al. (2021), highlighting the difference in isotopic signatures of dust exported from some of Earth's most important dust producing regions.

Radiogenic isotope data on unconsolidated sediments from active dust source areas in Mesopotamia are sparse but there is some coverage (Figure 8, Supplementary Table 3). More data are needed to accurately characterise this region but, based on the information available, our DSAF-weighted mean Sr and Nd isotopic compositions for the Mesopotamian PSA ($^{87}Sr/^{86}Sr$ 0.7087 ± 0.0017; ε_{Nd} -3.5 ± 1.8) fall between those of the Eastern Sahara and of the central belt of the Arabian Peninsula and Southern Levant (Figures 7, 8 and 9). We find that, despite its proximity to northern Mesopotamia, the geochemical signature of surface sediment samples from Southern Levant PSA more closely resembles that of the more distant Arabian Peninsula PSA (Figures 7, 8 and 9). This result emphasises the strong imprint of the Tigris-Euphrates River system on dust source composition in Mesopotamia. This result supports our decision to define separate PSAs (Mesopotamia and Southern Levant, Figure 4) even though, at the spatial scale of the remotely sensed data, they appear as one contiguous region in the DSAF data (Figure 5).

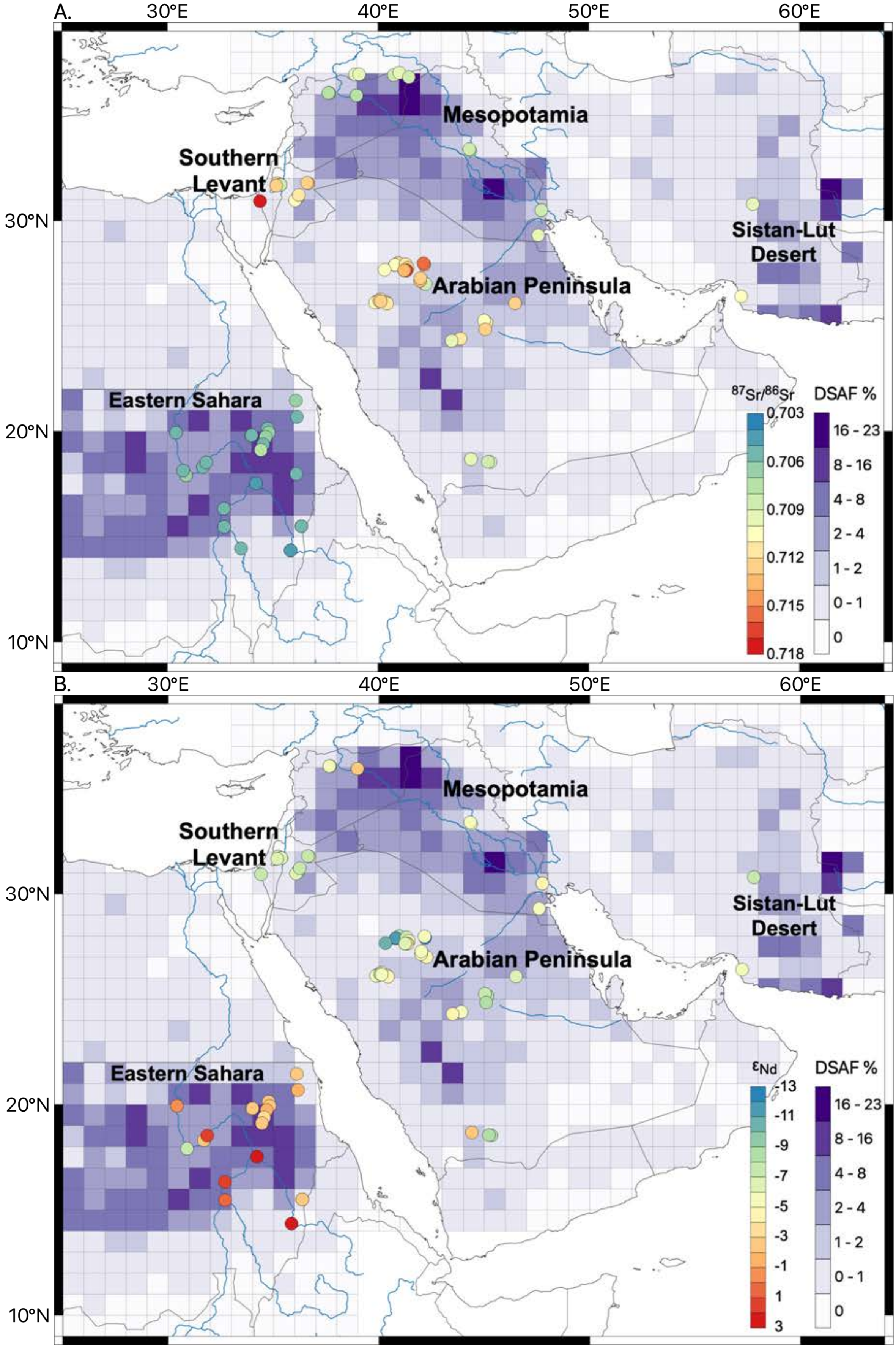
A.
30°E
40°E
50°E
60°E
30°N
20°N
10°N
Mesopotamia
Southern
Levant
Sistan-Lut
Desert
Arabian Peninsula
Eastern Sahara
$^{87}Sr/^{86}Sr$
0.703
0.706
0.709
0.712
0.715
0.718
DSAF %
16 - 23
8 - 16
4 - 8
2 - 4
1 - 2
0 - 1
0
B.
30°E
40°E
50°E
60°E
30°N
20°N
10°N
Mesopotamia
Southern
Levant
Sistan-Lut
Desert
Arabian Peninsula
Eastern Sahara
ε_{Nd}
-13
-11
-9
-7
-5
-3
-1
1
3
DSAF %
16 - 23
8 - 16
4 - 8
2 - 4
1 - 2
0 - 1
0

Figure 8. Spatial coverage of new and previously published isotope data from unconsolidated surface sediment samples overlain on annual DSAF maps. Isotope composition of individual data points is indicated by colour (scale bar shown): $^{87}Sr/^{86}Sr$ (A) and ε_{Nd} (B). Dust source activation frequency (DSAF) as in Figure 5. Major rivers and wadis are shown in blue.

The isotopic signature of a surface soil sample from the Iranian Persian Gulf coast (SR-8, 0.71094 and -5.8 for $^{87}Sr/^{86}Sr$ and ε_{Nd}, respectively) reported by Kumar et al., (2020) (Figure 8) aligns well with the composition that we report for a yardang sample from the Lut Desert (0.70965 and -7.7 for $^{87}Sr/^{86}Sr$ and ε_{Nd}, respectively). However, to our knowledge, there are no other published radiogenic isotope data on unconsolidated sediments from active dust source areas in Iran. The coastal sample is not optimally located for our purposes (Figure 8) but, due to the sparsity of available data, we combine it with our yardang sample to define a preliminary signature for the Sistan-Lut Desert PSA. These two measurements of unconsolidated sediments are isotopically distinct from the majority of data of volcanic rocks in the region, which range between 0.70389 and 0.70836 (mean, 0.7056) in $^{87}Sr/^{86}Sr$ and between -5.9 to 3.7 in ε_{Nd} (mean, 0.4). They also lie just outside the range of aerosols collected in Goa, India which have been used to infer dust sourced from the Sistan-Lut basin region: $^{87}Sr/^{86}Sr$ between 0.70494 and 0.71938 and ε_{Nd} between -7.9 and -12.8 (Supplementary Table 3 and Supplementary Figure 1) (Kumar et al., 2020; Suresh et al., 2021). Suresh et al., (2021) suggest that the isotopic spread in aerosol samples from the Sistan-Lut basin reflects the heterogeneity of dust sources, but other factors such as mixing of dust during transport and limitations of tracking dust from source-to-sink using satellite imagery and air mass back trajectory analyses may also play a role. More data are needed from Iran to confidently define a PSA signature, but our observations indicate that non-volcanic sources have a major influence on dust composition in the Sistan-Lut Desert (Figure 4) and the discrepancies between sediment and aerosol isotopic values when Sr and Nd are considered together (Supplementary Figure 1) suggest that further work is needed to better understand provenance of the aerosol samples collected in Goa.

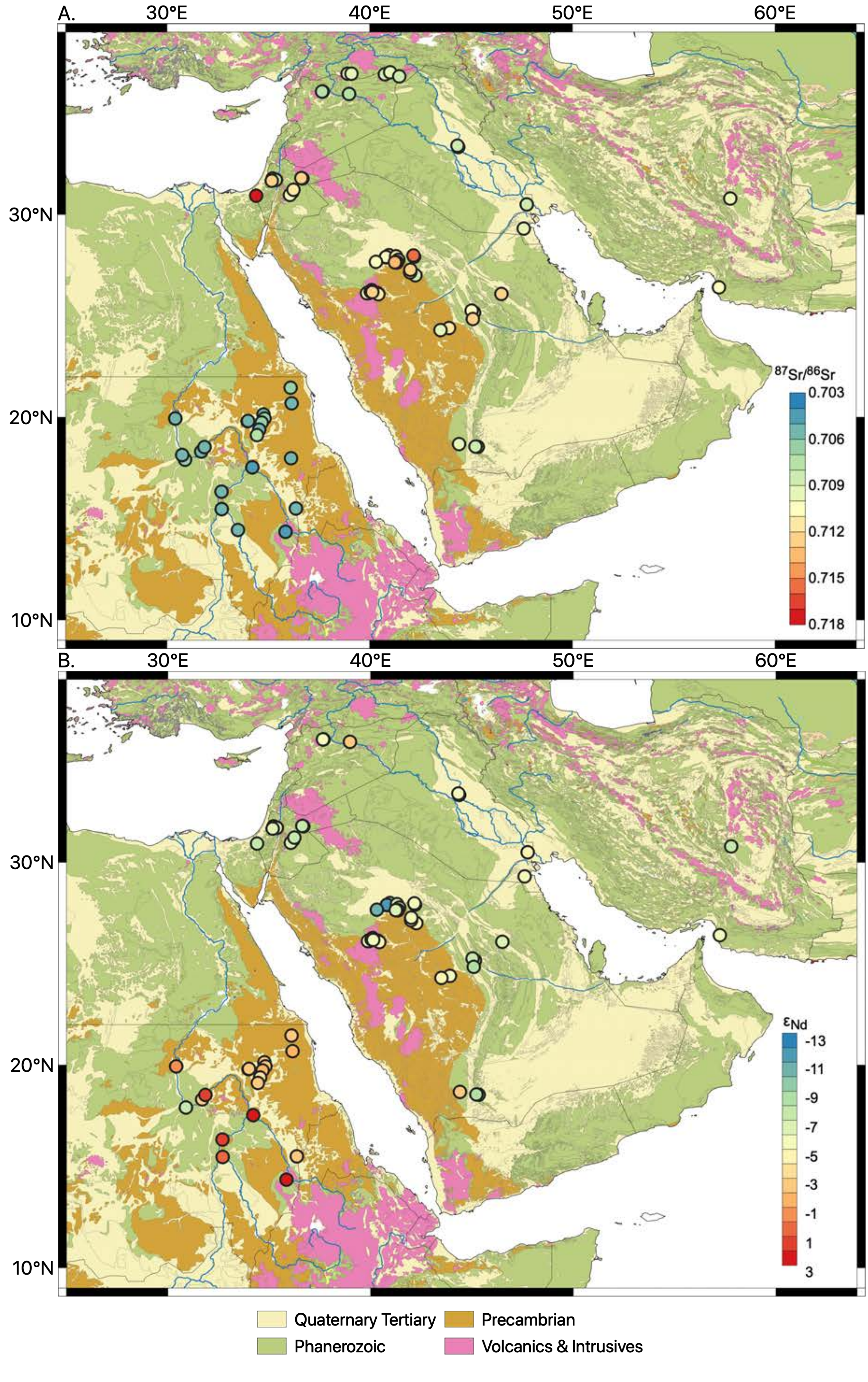
A.
30°E
40°E
50°E
60°E
30°N
20°N
10°N
$^{87}Sr/^{86}Sr$
0.703
0.706
0.709
0.712
0.715
0.718
B.
ε_{Nd}
-13
-11
-9
-7
-5
-3
-1
1
3
Quaternary Tertiary
Precambrian
Phanerozoic
Volcanics & Intrusives

663

Figure 9. Simplified geological map overlain with new and previously published radiogenic isotope data. $^{87}Sr/^{86}Sr$ (A.) and ε_{Nd} (B.) signatures of unconsolidated sediments (circles) are indicated by colour (scale bar shown). Major river systems shown in blue, national boundaries in grey. Geological map adapted from Pawlewicz et al., 2002; Persits et al., 1997, 1999; Pollastro et al., 1997, 1999.

4.2.2 The influence of grain size on radiogenic isotope signatures

Tracing dust provenance relies on matching the isotopic composition of source material with aerosols and/or terrigenous deposits in marine and lake sediments. Therefore, it is important to understand the secondary processes that can influence isotopic signatures from source to sink. These include chemical weathering of source rock as well as grain-size sorting during wind and fluvial transport (Fralick and Kronberg, 1997). Typically, Nd isotopes are considered not to undergo major fractionation during weathering and transport (Feng et al., 2009; Grousset et al., 1992). On the other hand, fractionation during weathering and transport is often inferred for Sr isotopes and typically results in higher $^{87}Sr/^{86}Sr$ with increasing weathering intensity and decreasing grain size (Bayon et al., 2021; Feng et al., 2009; Grousset et al., 1992; Meyer et al., 2011). To assess the importance of these processes, we analysed five different grain size fractions: <4 µm, 4-15 µm, 15- 32 µm, 32-45 µm and 45-63 µm for five representative samples from the Arabian Peninsula and Southern Levant (Figure 10, Supplementary Table 2).

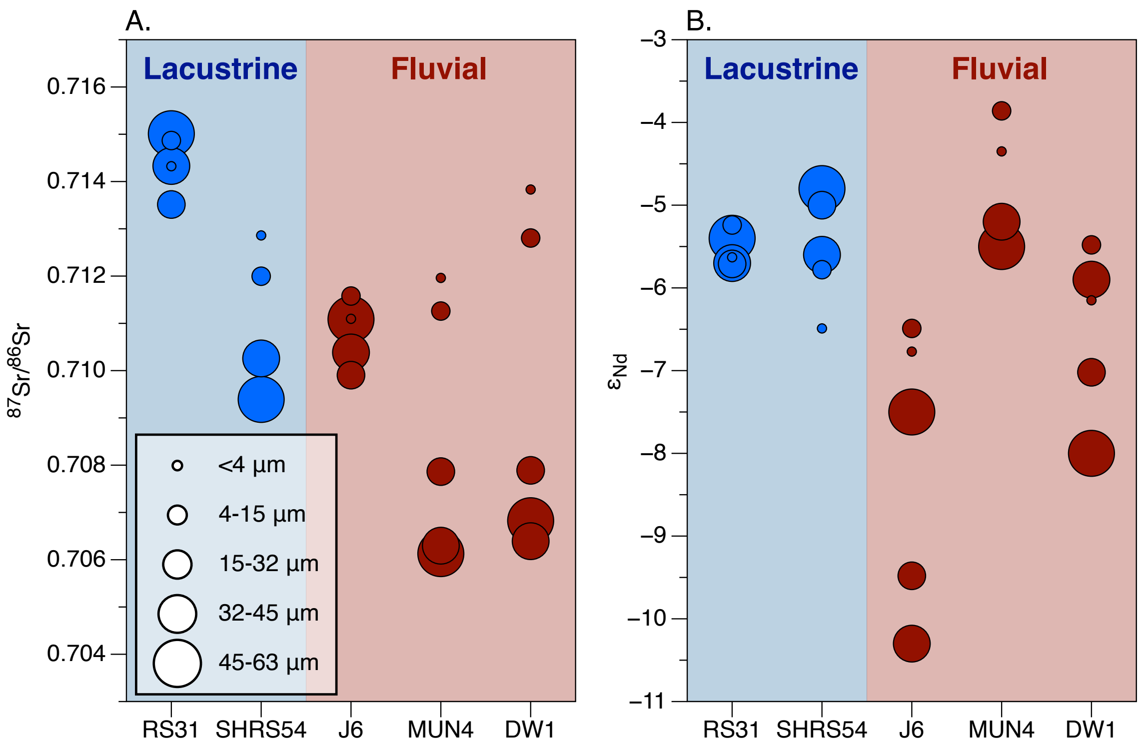

Figure 10. The relationship between grain size and isotopic composition of five representative samples from the central belt of the Arabian Peninsula and Southern Levant (RS31, SHRS5, J6, MUN4 and DW1 for locations see Figure 4). The distribution of $^{87}Sr/^{86}Sr$ (A) and ε_{Nd} (B) for lacustrine samples (RS31 and SHRS54, blue) and fluvial samples (MUN4, J6 and DW1, red). Size of the symbol indicates size fraction (<4 µm, 4-15 µm, 15- 32 µm, 32-45 µm and 45-63 µm) from smallest to largest.

Samples from dried lake beds (RS31 and SHRS54) show less variability in either Sr or Nd isotopic signature between grain size fractions than those from dried riverbeds (Figure 10). The riverbed samples (J6, DW1, MUN4) show substantial grain-size dependent isotopic fractionation in both Sr and Nd, especially in the less than 15 µm fraction (Figure 10). More data are needed to fully understand these isotopic offsets with grain size, but they are consistent with the results of Jewell et al., (2021) from Africa and suggest that transport history and changes in regional geology downstream associated with the chemical maturity of the sediments (Bayon et al., 2021) play an important role. Regardless, our results underscore the importance of a consistent approach to sampling and analysis, even for ε_{Nd}, especially in regions that are geologically complex and isotopically diverse.

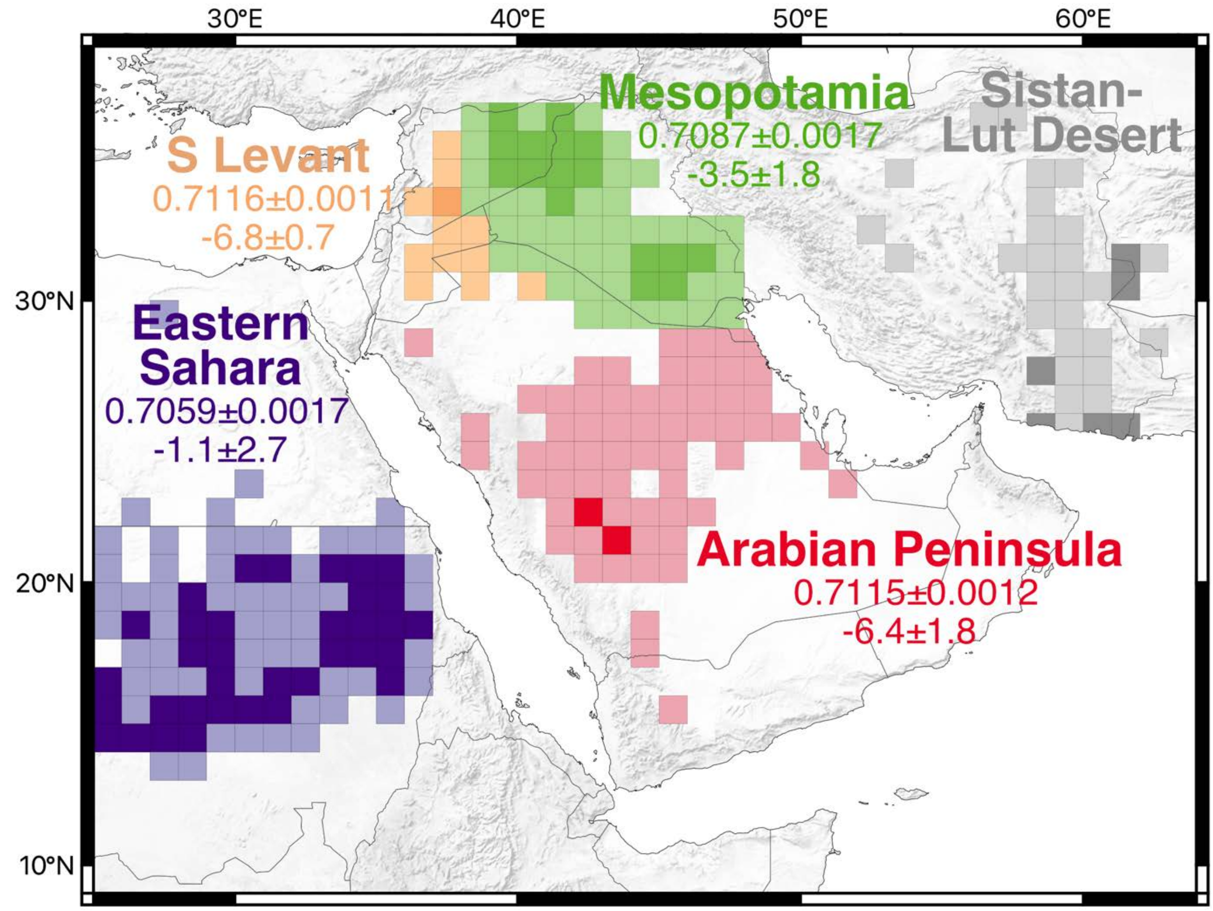

Figure 11. Overview of the weighted means (± 1sd) of $^{87}Sr/^{86}Sr$ and ε_{Nd} of unconsolidated surface sediments in preferential source areas of dust generation: Eastern Sahara (purple, Jewell et al. 2021), central belt of the Arabian Peninsula (red), Southern Levant (orange) and Mesopotamia (green). Dust map for Eastern Sahara (Schepanski et al., 2012), the Arabian Peninsula and SW Asia (Hennen, 2017) indicates the DSAF (%) of >5 % (dark colours) and 1-5 % (pale colours).

5 CONCLUSIONS

We combine satellite and radiogenic isotope data to identify and geochemically characterise three preferential source areas (PSAs) of dust generation in Westernmost Asia: i) the central belt of the Arabian Peninsula, ii) Mesopotamia and iii) the Southern Levant. With further work, the Sistan-Lut Desert dust producing region in Iran may also be distinguished isotopically. Following the approach of Jewell et al., (2021), we characterize these PSAs geochemically using Sr and Nd isotope data, targeting our sampling at dust-producing hot spots in dried river and lake beds. We weight our geochemical data by local dust source activation frequency to produce representative estimates of the isotopic signature of emitted dust. We show that the main dust sources of Westernmost Asia have geochemical fingerprints that can be readily distinguished from dust sourced from the Sahara (Figures 7 and 11). More data are needed from dust-producing sites in Mesopotamia and the deserts of Iran to better constrain the geochemical fingerprints of those regions.

We find that sediment transport mechanisms exert differing controls over dust source isotopic signatures in West Asia and the Sahara. Long-range sediment transport by both the Nile and its tributaries and the Tigris-Euphrates river system exerts a strong influence on the geochemical fingerprint of dust sources in the Eastern Sahara and Mesopotamia respectively (Figure 5 and 11). One consequence of this long-range transport is that the dust sources of Mesopotamia are readily distinguished geochemically from those of the Southern Levant despite the proximity of these two PSAs (Figure 5 and 11). Another consequence is the influence of the Ethiopian Highlands on the geochemical fingerprint of the Eastern Sahara. Even in the central Arabian Peninsula where there is no major long-range riverine transport of sediments to consider, the correspondence between dust sources and the underlying bedrock geology of the Arabian Nubian Shield is not particularly strong. This observation suggests long intervals of palaeo aridity and spatially extensive and effective mixing by aeolian transport internally (see Figure 9 and discussion in section 4.2.1). We identify a secondary influence of grain size on both Sr and Nd isotopes from sediment samples collected in palaeoriver deposits, but this effect is much smaller in sediments sampled from palaeolakes. Our analysis provides an improved framework for tracing dust from source-to-sink over long distances, a prerequisite for successfully interpreting records of palaeoclimate variability.

Acknowledgements

This work was supported by the Natural Environment Research Council (NERC) [studentship number NE/L002531/1 to TK] and by a Royal Society Challenge Grant CH160073, a Royal Society Wolfson Merit Award to PAW and a University of Southampton GCRF award to PAW and AJC. Research by PSB utilised in this paper was funded by the Leverhulme Trust (ECF-2019-538) and NERC (NE/J500306/1). We acknowledge the support of the Heritage Commission, Saudi Ministry of Culture, and the Max Planck Society for field research in the Kingdom of Saudi Arabia. We thank Charlie Bristow for stimulating discussions and sample acquisition, Kevin White (the University of Reading) for help with accessing the remote sensing data, Jani Radebaugh for help with sample acquisition, Amelia Gale, Megan Wilding, Sarge Bray and Bastian Hambach for laboratory assistance. We thank Steve Bohaty, Kerstin Schepanski, Werner Ehrmann, Clive Gamble, Huw Groucutt, Ellie Pryor and Ellie Scerri for stimulating discussions. We are grateful to Adi Torfstein, an anonymous reviewer and editor Miryam Bar-Matthews for constructive comments that significantly improved this contribution.

Appendix A. Supplementary material

Supplementary Table 1. Annual and seasonal dust source activation frequency data (DSAF, %).

*Supplementary Table 2. List of samples in this study. Samples marked with * were measured at 63-45 µm, 45 -32µm and <32 µm discussed in more detail in section 0.*

Supplementary Table 3. A list of published sediment and aerosol samples from Southern Levant, Mesopotami and Sistan-Lut Desert used in our compilation including the Sr and Nd isotopic values, sample descriptions, location and grain size fraction used for analysis.

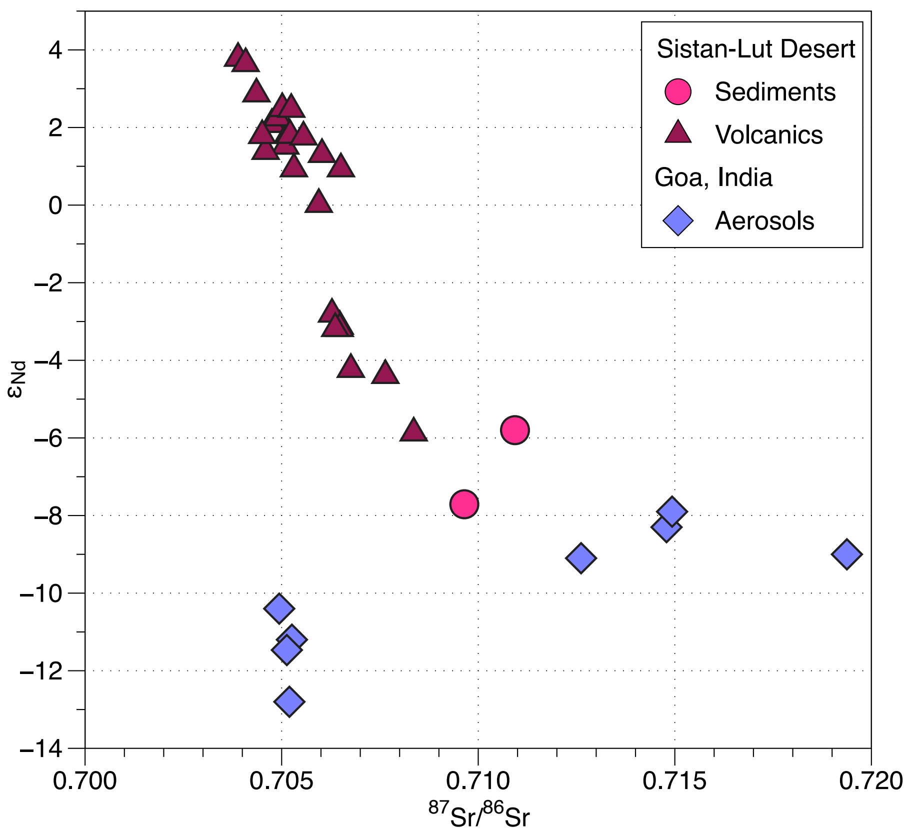

Supplementary Figure 1. Comparison of Sr and Nd isotopic composition within Sistan-Lut Desert PSA: (i) surface sediments (pink circles), (ii) volcanic rocks (dark red triangles) (Arjmandzadeh and Santos, 2014; Pang et al., 2014; Saadat et al., 2010) *and (iii) aerosols collected in Goa, India (blue diamonds)* (Kumar et al., 2020; Suresh et al., 2021) .

Reference List

Aarons, S.M., Blakowski, M.A., Aciego, S.M., Stevenson, E.I., Sims, K.W.W., Scott, S.R., Aarons, C., 2017. Geochemical characterization of critical dust source regions in the American West. Geochim. Cosmochim. Acta 215, 141–161. https://doi.org/10.1016/j.gca.2017.07.024

Abouchami, W., Näthe, K., Kumar, A., Galer, S.J.G., Jochum, K.P., Williams, E., Horbe, A.M.C., Rosa, J.W.C., Balsam, W., Adams, D., Mezger, K., Andreae, M.O., 2013. Geochemical and isotopic characterization of the bodele depression dust source and implications for transatlantic dust transport to the Amazon basin. Earth Planet. Sci. Lett. 380, 112–123. https://doi.org/10.1016/j.epsl.2013.08.028

Altherr, R., Henjes-Kunst, F., Baumann, A., 1990. Asthenosphere versus lithosphere as possible sources for basaltic magmas erupted during formation of the Red Sea: constraints from Sr, Pb and Nd isotopes. Earth Planet. Sci. Lett. 96, 269–286. https://doi.org/10.1016/0012-821X(90)90007-K

Altherr, R., Mertz-Kraus, R., Volker, F., Kreuzer, H., Henjes-Kunst, F., Lange, U., 2019. Geodynamic setting of Upper Miocene to Quaternary alkaline basalts from Harrat al ‘Uwayrid (NW Saudi Arabia): Constraints from K–Ar dating, chemical and Sr-Nd-Pb isotope compositions, and petrological modeling. Lithos 330–331, 120–138. https://doi.org/10.1016/j.lithos.2019.02.007

Arjmandzadeh, R., Santos, J.F., 2014. Sr-Nd isotope geochemistry and tectonomagmatic setting of the Dehsalm Cu-Mo porphyry mineralizing intrusives from Lut Block, eastern Iran. Int. J. Earth Sci. 103, 123–140. https://doi.org/10.1007/s00531-013-0959-4

Bakker, N.L., Drake, N.A., Bristow, C.S., 2019. Evaluating the relative importance of northern African mineral dust sources using remote sensing. Atmos. Chem. Phys. 19, 10525–10535. https://doi.org/10.5194/acp-19-10525-2019

Bastian, L., Mologni, C., Vigier, N., Bayon, G., Lamb, H., Bosch, D., Kerros, M.E., Colin, C., Revel, M., 2021. Co-variations of climate and silicate weathering in the Nile Basin during the Late Pleistocene. Quat. Sci. Rev. 264, 107012. https://doi.org/10.1016/j.quascirev.2021.107012

Bayon, G., Freslon, N., Germain, Y., Bindeman, I.N., Trinquier, A., Barrat, J.A., 2021. A global survey of radiogenic strontium isotopes in river sediments. Chem. Geol. 559, 119958. https://doi.org/10.1016/j.chemgeo.2020.119958

Bayon, G., German, C.R., Boella, R.M., Milton, J.A., Taylor, R.N., Nesbitt, R.W., 2002. An improved method for extracting marine sediment fractions and its application to Sr and Nd isotopic analysis. Chem. Geol. 187, 179–199. https://doi.org/10.1016/S0009-2541(01)00416-8

Bayon, G., Toucanne, S., Skonieczny, C., André, L., Bermell, S., Cheron, S., Dennielou, B., Etoubleau, J., Freslon, N., Gauchery, T., Germain, Y., Jorry, S.J., Ménot, G., Monin, L., Ponzevera, E., Rouget, M.L., Tachikawa, K., Barrat, J.A., 2015. Rare earth elements and neodymium isotopes in world river sediments revisited. Geochim. Cosmochim. Acta 170, 17–38. https://doi.org/10.1016/j.gca.2015.08.001

Begg, G.C., Griffin, W.L., Natapov, L.M., O'Reilly, S.Y., Grand, S.P., O'Neill, C.J., Hronsky, J.M.A., Djomani, Y.P., Swain, C.J., Deen, T., Bowden, P., 2009. The lithospheric architecture of Africa: Seismic tomography, mantle petrology, and tectonic evolution. Geosphere 5, 23–50. https://doi.org/10.1130/GES00179.1

Ben Israel, M., Enzel, Y., Amit, R., Erel, Y., 2015. Provenance of the various grain-size fractions in the Negev loess and potential changes in major dust sources to the Eastern Mediterranean. Quat. Res. (United States) 83, 105–115. https://doi.org/10.1016/j.yqres.2014.08.001

Betzler, C., Eberli, G.P., Kroon, D., Wright, J.D., Swart, P.K., Nath, B.N., Alvarez-Zarikian, C.A., Alonso-Garciá, M., Bialik, O.M., Blättler, C.L., Guo, J.A., Haffen, S., Horozal, S., Inoue, M., Jovane, L., Lanci, L., Laya, J.C., Mee, A.L.H., Lüdmann, T., Nakakuni, M., Niino, K., Petruny, L.M., Pratiwi, S.D., Reijmer, J.J.G., Reolid, J., Slagle, A.L., Sloss, C.R., Su, X., Yao, Z., Young, J.R., 2016. The abrupt onset of the modern South Asian Monsoon winds. Sci. Rep. 6, 1–10. https://doi.org/10.1038/srep29838

Bialik, O.M., Auer, G., Ogawa, N.O., Kroon, D., Waldmann, N.D., Ohkouchi, N., 2020. Monsoons, Upwelling, and the Deoxygenation of the Northwestern Indian Ocean in Response to Middle to Late Miocene Global Climatic Shifts. Paleoceanogr.

Paleoclimatology 35, 1–17. https://doi.org/10.1029/2019PA003762
Bodenheimer, S., Lensky, I.M., Dayan, U., 2019. Characterization of Eastern Mediterranean dust storms by area of origin; North Africa vs. Arabian Peninsula. Atmos. Environ. 198, 158–165. https://doi.org/10.1016/j.atmosenv.2018.10.034
Breeze, P.S., Drake, N.A., Groucutt, H.S., Parton, A., Jennings, R.P., White, T.S., Clark-Balzan, L., Shipton, C., Scerri, E.M.L., Stimpson, C.M., Crassard, R., Hilbert, Y., Alsharekh, A., Al-Omari, A., Petraglia, M.D., 2015. Remote sensing and GIS techniques for reconstructing Arabian palaeohydrology and identifying archaeological sites. Quat. Int. 382, 98–119. https://doi.org/10.1016/j.quaint.2015.01.022
Bullard, J.E., Harrison, S.P., Baddock, M.C., Drake, N., Gill, T.E., McTainsh, G., Sun, Y., 2011. Preferential dust sources: A geomorphological classification designed for use in global dust-cycle models. J. Geophys. Res. Earth Surf. 116. https://doi.org/10.1029/2011JF002061
Burg, J.P., 2018. Geology of the onshore Makran accretionary wedge: Synthesis and tectonic interpretation. Earth-Science Rev. 185, 1210–1231. https://doi.org/10.1016/j.earscirev.2018.09.011
Chen, J., Li, G., Yang, J., Rao, W., Lu, H., Balsam, W., Sun, Y., Ji, J., 2007. Nd and Sr isotopic characteristics of Chinese deserts: Implications for the provenances of Asian dust. Geochim. Cosmochim. Acta 71, 3904–3914. https://doi.org/10.1016/j.gca.2007.04.033
Clemens, S.C., Murray, D.W., Prell, W.L., 1996. Nonstationary phase of the plio-pleistocene Asian monsoon. Science (80-.). 274, 943–948.
Clift, P.D., Zhou, P., Stockli, D.F., Blusztajn, J., 2019. Regional Pliocene exhumation of the Lesser Himalaya in the Indus drainage. Solid Earth 10, 647–661. https://doi.org/10.5194/se-10-647-2019

Crocker, A.J., Naafs, B.D.A., Westerhold, T., James, R.H., Cooper, M.J., Röhl, U., Pancost, R.D., Xuan, C., Osborne, C.P., Beerling, D.J., Wilson, P.A., 2022. Astronomically controlled aridity in the Sahara since at least 11 million years ago. Nat. Geosci. https://doi.org/10.1038/s41561-022-00990-7

DeMenocal, P.B., 2004. African climate change and faunal evolution during the Pliocene - Pleistocene. Earth Planet. Sci. Lett. 220. https://doi.org/10.1016/S0012-821X(04)00003-2

Ehrmann, W., Schmiedl, G., 2021. Nature and dynamics of North African humid and dry periods during the last 200,000 years documented in the clay fraction of eastern mediterranean deep-sea sediments. Quat. Sci. Rev. 260, 106925. https://doi.org/10.1016/j.quascirev.2021.106925

Enzel, Y., Kushnir, Y., Quade, J., 2015. The middle Holocene climatic records from Arabia: Reassessing lacustrine environments, shift of ITCZ in Arabian Sea, and impacts of the southwest Indian and African monsoons. Glob. Planet. Change 129, 69–91. https://doi.org/10.1016/j.gloplacha.2015.03.004

Feng, J.L., Zhu, L.P., Zhen, X.L., Hu, Z.G., 2009. Grain size effect on Sr and Nd isotopic compositions in eolian dust: Implications for tracing dust provenance and Nd model age. Geochem. J. 43, 123–131. https://doi.org/10.2343/geochemj.1.0007

Fleitmann, D., Burns, S.J., Pekala, M., Mangini, A., Al-Subbary, A.A., Al-Aowah, M., Kramers, J., Matter, A., 2011. Holocene and Pleistocene pluvial periods in Yemen, southern Arabia. Quat. Sci. Rev. 30, 783–787. https://doi.org/10.1016/j.quascirev.2011.01.004

Fleitmann, D., Haldon, J., Bradley, R.S., Burns, S.J., Cheng, H., Edwards, R.L., Raible, C.C., Jacobson, M., Matter, A., 2022. Droughts and societal change: The environmental context for the emergence of Islam in late Antique Arabia. Science (80-.). 376, 1317–

1321. https://doi.org/10.1126/science.abg4044

Fralick, P.W., Kronberg, B.I., 1997. Geochemical discrimination of elastic sedimentary rock sources. Sediment. Geol. 113, 111–124.

Gherboudj, I., Naseema Beegum, S., Ghedira, H., 2017. Identifying natural dust source regions over the Middle-East and North-Africa: Estimation of dust emission potential. Earth-Science Rev. 165, 342–355. https://doi.org/10.1016/j.earscirev.2016.12.010

Ginoux, P., Prospero, J.M., Gill, T.E., Hsu, N.C., Zhao, M., 2012. Global-scale attribution of anthropogenic and natural dust source and their emission rates based on MODIS deep blue aerosol products. Rev. Geophys. 50, 1–36. https://doi.org/10.1029/2012RG000388.1.INTRODUCTION

Ginoux, P., Prospero, J.M., Torres, O., Chin, M., 2004. Long-term simulation of global dust distribution with the GOCART model: Correlation with North Atlantic Oscillation. Environ. Model. Softw. 19, 113–128. https://doi.org/10.1016/S1364-8152(03)00114-2

Grant, K.M., Rohling, E.J., Westerhold, T., Zabel, M., Heslop, D., Konijnendijk, T.Y.M., Lourens, L.J., 2017. A 3 million year index for North African humidity/aridity and the implication of potential pan-African Humid periods. Quat. Sci. Rev. 171, 100–118. https://doi.org/10.1016/j.quascirev.2017.07.005

Groucutt, H.S., White, T.S., Scerri, E.M.L., Andrieux, E., Clark-Wilson, R., Breeze, P.S., Armitage, S.J., Stewart, M., Drake, N., Louys, J., Price, G.J., Duval, M., Parton, A., Candy, I., Carleton, W.C., Shipton, C., Jennings, R.P., Zahir, M., Blinkhorn, J., Blockley, S., Al-Omari, A., Alsharekh, A.M., Petraglia, M.D., 2021. Multiple hominin dispersals into Southwest Asia over the past 400,000 years. Nature 597, 376–380. https://doi.org/10.1038/s41586-021-03863-y

Grousset, F.E., Rognon, P., Coudé-Gaussen, G., Pédemay, P., 1992. Origins of peri-Saharan dust deposits traced by their Nd and Sr isotopic composition. Palaeogeogr.

Palaeoclimatol. Palaeoecol. 93, 203–212. https://doi.org/10.1016/0031-0182(92)90097-O

Haliva-Cohen, A., Stein, M., Goldstein, S.L., Sandler, A., Starinsky, A., 2012. Sources and transport routes of fine detritus material to the Late Quaternary Dead Sea basin. Quat. Sci. Rev. 50, 55–70. https://doi.org/10.1016/j.quascirev.2012.06.014

Hartman, A., Torfstein, A., Almogi-Labin, A., 2020. Climate swings in the northern Red Sea over the last 150,000 years from εNd and Mg/Ca of marine sediments. Quat. Sci. Rev. 231, 106205. https://doi.org/10.1016/J.QUASCIREV.2020.106205

Henderson, J., Ma, H., Evans, J., 2020. Glass production for the Silk Road? Provenance and trade of islamic glasses using isotopic and chemical analyses in a geological context. J. Archaeol. Sci. 119. https://doi.org/10.1016/j.jas.2020.105164

Hennen, M., 2017. Characterisation of mineral dust emission in the Middle East using Remote Sensing techniques. University of Reading.

Hersbach, H., Bell, B., Berrisford, P., Hirahara, S., Horányi, A., Muñoz-Sabater, J., Nicolas, J., Peubey, C., Radu, R., Schepers, D., Simmons, A., Soci, C., Abdalla, S., Abellan, X., Balsamo, G., Bechtold, P., Biavati, G., Bidlot, J., Bonavita, M., De Chiara, G., Dahlgren, P., Dee, D., Diamantakis, M., Dragani, R., Flemming, J., Forbes, R., Fuentes, M., Geer, A., Haimberger, L., Healy, S., Hogan, R.J., Hólm, E., Janisková, M., Keeley, S., Laloyaux, P., Lopez, P., Lupu, C., Radnoti, G., de Rosnay, P., Rozum, I., Vamborg, F., Villaume, S., Thépaut, J.N., 2020. The ERA5 global reanalysis. Q. J. R. Meteorol. Soc. 146, 1999–2049. https://doi.org/10.1002/qj.3803

Huang, Y., Clemens, S.C., Liu, W., Wang, Y., Prell, W.L., 2007. Large scale hydrological change drove the late miocene C4 plant expansion in the Himalayan foreland Arabian Peninsula. Geology 35, 531–534. https://doi.org/10.1130/G23666A.1

Inness, A., Ades, M., Agustí-Panareda, A., Barr, J., Benedictow, A., Blechschmidt, A.M., Jose Dominguez, J., Engelen, R., Eskes, H., Flemming, J., Huijnen, V., Jones, L., Kipling, Z., Massart, S., Parrington, M., Peuch, V.H., Razinger, M., Remy, S., Schulz, M., Suttie, M., 2019. The CAMS reanalysis of atmospheric composition. Atmos. Chem. Phys. 19, 3515–3556. https://doi.org/10.5194/acp-19-3515-2019

Jacobsen, S.B., Wasserburg, G.J., 1980. Sm-Nd isotopic evolution of chondrites. Earth Planet. Sci. Lett. 50, 139–155. https://doi.org/10.1016/0012-821X(80)90125-9

Jardine, G.E., Crocker, A.J., Bailey, I., Cooper, M.J., Milton, J.A., Wilson, P.A., 2021. The imprint of dust from the North American Southwest on the California Channel Islands and Pacific Ocean sediments. Quat. Sci. Rev. 106934.

Jewell, A.M., Cooper, M.J., Milton, J.A., James, R.H., Crocker, A.J., Wilson, P.A., 2022. Chemical isolation and isotopic analysis of terrigenous sediments with emphasis on effective removal of contaminating marine phases including barite. Chem. Geol. 589, 120673. https://doi.org/10.1016/j.chemgeo.2021.120673

Jewell, A.M., Drake, N., Crocker, A.J., Bakker, N.L., Kunkelova, T., Bristow, C.S., Cooper, M.J., Milton, J.A., Breeze, P.S., Wilson, P.A., 2021. Three North African Dust Source Areas and their Geochemical Fingerprint. Earth Planet. Sci. Lett. 554, 116645. https://doi.org/https://doi.org/10.1016/j.epsl.2020.116645

Jickells, T.D., An, Z.S., Andersen, K.K., Baker, A.R., Bergametti, G., Brooks, N., Cao, J.J., Boyd, P.W., Duce, R.A., Hunter, K.A., Kawahata, H., Kubilay, N., LaRoche, J., Liss, P.S., Mahowald, N., Prospero, J.M., Ridgwell, A.J., Tegen, I., Torres, R., 2005. Global Iron Connections Between Desert Dust, Ocean Biogeochemistry, and Climate. Science (80-.). 308, 67–72.

Kaskaoutis, D.G., Rashki, A., Houssos, E.E., Legrand, M., Francois, P., Bartzokas, A., Kambezidis, H.D., Dumka, U.C., Goto, D., Takemura, T., 2017. Assessment of changes in atmospheric dynamics and dust activity over southwest Asia using the Caspian Sea–

Hindu Kush Index. Int. J. Climatol. 37, 1013–1034. https://doi.org/10.1002/joc.5053

Kaufman, Y.J., Koren, I., Remer, L.A., Rosenfeld, D., Rudich, Y., 2005. The effect of smoke, dust, and pollution aerosol on shallow cloud development over the Atlantic Ocean. Proc. Natl. Acad. Sci. U. S. A. 102, 11207–11212. https://doi.org/10.1073/pnas.0505191102

Khaniabadi, Y.O., Daryanoosh, S.M., Amrane, A., Polosa, R., Hopke, P.K., Goudarzi, G., Mohammadi, M.J., Sicard, P., Armin, H., 2017. Impact of Middle Eastern Dust storms on human health. Atmos. Pollut. Res. 8, 606–613. https://doi.org/10.1016/j.apr.2016.11.005

Kibaroğlu, M., Falb, C., Hartmann, G., 2017. Application of strontium isotope analysis to provenance studies of Early Bronze Age North-Mesopotamian Metallic Ware. J. Archaeol. Sci. Reports 16, 573–588. https://doi.org/10.1016/j.jasrep.2017.09.024

Kröner, A., Linnebacher, P., Stern, R.J., Reischmann, T., Manton, W., Hussein, I.M., 1991. Evolution of Pan-African island arc assemblages in the southern Red Sea Hills, Sudan, and in southwestern Arabia as exemplified by geochemistry and geochronology. Precambrian Res. 53, 99–118. https://doi.org/10.1016/0301-9268(91)90007-W

Kroon, D., Steens, T., Troelstra, S.R., 1991. Onset of monsoonal related upwelling in the western Arabian sea as revealed by planktonic foraminifers. Proc. Ocean Drill. Program, Sci. Results 117, 257–263. https://doi.org/10.2973/odp.proc.sr.117.126.1991

Kumar, A., Suresh, K., Rahaman, W., 2020. Geochemical characterization of modern aeolian dust over the Northeastern Arabian Sea: Implication for dust transport in the Arabian Sea. Sci. Total Environ. 729, 138576. https://doi.org/10.1016/j.scitotenv.2020.138576

Kutuzov, S., Legrand, M., Preunkert, S., Ginot, P., Mikhalenko, V., Shukurov, K., Poliukhov, A., Toropov, P., 2019. The Elbrus (Caucasus, Russia) ice core record-Part 2: History of desert dust deposition. Atmos. Chem. Phys. 19, 14133–14148. https://doi.org/10.5194/acp-19-14133-2019

Matter, A., Neubert, E., Preusser, F., Rosenberg, T., Al-Wagdani, K., 2015. Palaeo-environmental implications derived from lake and sabkha deposits of the southern Rub' al-Khali, Saudi Arabia and Oman. Quat. Int. 382, 120–131. https://doi.org/10.1016/j.quaint.2014.12.029

McGee, D., Broecker, W.S., Winckler, G., 2010. Gustiness: The driver of glacial dustiness? Quat. Sci. Rev. 29, 2340–2350. https://doi.org/10.1016/j.quascirev.2010.06.009

Meyer, I., Davies, G.R., Stuut, J.B.W., 2011. Grain size control on Sr-Nd isotope provenance studies and impact on paleoclimate reconstructions: An example from deep-sea sediments offshore NW Africa. Geochemistry, Geophys. Geosystems 12, 1–14. https://doi.org/10.1029/2010GC003355

Middleton, N., 2019. Variability and Trends in Dust Storm Frequency on Decadal Timescales: Climatic Drivers and Human Impacts. Geosciences 9. https://doi.org/doi:10.3390/geosciences9060261

Moore, C.M., Mills, M.M., Arrigo, K.R., Berman-Frank, I., Bopp, L., Boyd, P.W., Galbraith, E.D., Geider, R.J., Guieu, C., Jaccard, S.L., Jickells, T.D., La Roche, J., Lenton, T.M., Mahowald, N.M., Marañón, E., Marinov, I., Moore, J.K., Nakatsuka, T., Oschlies, A., Saito, M.A., Thingstad, T.F., Tsuda, A., Ulloa, O., 2013. Processes and patterns of oceanic nutrient limitation. Nat. Geosci. 6, 701–710. https://doi.org/10.1038/ngeo1765

Nicholson, S.E., 2017. Climate and climatic variability of rainfall over eastern Africa. Rev. Geophys. 55, 590–635. https://doi.org/10.1002/2016RG000544

Nicholson, S.L., Pike, A.W.G., Hosfield, R., Roberts, N., Sahy, D., Woodhead, J., Cheng, H., Edwards, R.L., Affolter, S., Leuenberger, M., Burns, S.J., Matter, A., Fleitmann, D., 2020. Pluvial periods in Southern Arabia over the last 1.1 million-years. Quat. Sci. Rev. 229. https://doi.org/10.1016/j.quascirev.2019.106112

Padoan, M., Garzanti, E., Harlavan, Y., Villa, I.M., 2011. Tracing Nile sediment sources by

Sr and Nd isotope signatures (Uganda, Ethiopia, Sudan). Geochim. Cosmochim. Acta 75, 3627–3644. https://doi.org/10.1016/j.gca.2011.03.042

Palchan, D., Erel, Y., Stein, M., 2018a. Geochemical characterization of contemporary fine detritus in the Dead Sea watershed. Chem. Geol. 494, 30–42. https://doi.org/10.1016/j.chemgeo.2018.07.013

Palchan, D., Stein, M., Almogi-Labin, A., Erel, Y., Goldstein, S.L., 2013. Dust transport and synoptic conditions over the Sahara-Arabia deserts during the MIS6/5 and 2/1 transitions from grain-size, chemical and isotopic properties of Red Sea cores. Earth Planet. Sci. Lett. 382, 125–139. https://doi.org/10.1016/j.epsl.2013.09.013

Palchan, D., Stein, M., Goldstein, S.L., Almogi-Labin, A., Tirosh, O., Erel, Y., 2018b. Synoptic conditions of fine-particle transport to the last interglacial Red Sea-Dead Sea from Nd-Sr compositions of sediment cores. Quat. Sci. Rev. 179, 123–136. https://doi.org/10.1016/j.quascirev.2017.09.004

Palchan, D., Torfstein, A., 2019. A drop in Sahara dust fluxes records the northern limits of the African Humid Period. Nat. Commun. 10, 3803. https://doi.org/10.1038/s41467-019-11701-z

Pang, K.N., Chung, S.L., Zarrinkoub, M.H., Chiu, H.Y., Li, X.H., 2014. On the magmatic record of the Makran arc, southeastern Iran: Insights from zircon U-Pb geochronology and bulk-rock geochemistry. Geochemistry, Geophys. Geosystems 15, 3459–3475. https://doi.org/10.1002/2014GC005469.Received

Pastore, G., Baird, T., Vermeesch, P., Resentini, A., Garzanti, E., 2021. Provenance and recycling of Sahara Desert sand. Earth-Science Rev. 216, 103606. https://doi.org/10.1016/j.earscirev.2021.103606

Pawlewicz, M.J., Steinshouer, D.W., Gautier, D.L., 2002. Map Showing Geology, Oil and Gas Fields, and Geologic Provinces of Europe including Turkey. U.S. Geol. Surv. Open-

File Rep. 97-470-I 14.

Persits, F., Ahlbrandt, T.S., Tuttle, M.L., Charpentier, R.R., Brownfield, M.E., Takahashi, K.I., 1997. Map showing geology, oil and gas fields and geologic provinces of Africa. U.S. Geol. Surv. Open-File Rep. 97-470-A. https://doi.org/https://doi.org/10.3133/ofr97470A

Persits, F.M., Ulmishek, G.F., Steinshouer, D.W., 1999. Maps showing geology, oil and gas fields and geologic provinces of the former Soviet Union. U.S. Geol. Surv. Open-File Rep. 97-470-E 13. https://doi.org/https://doi.org/10.3133/ofr97470E

Petraglia, M.D., 2005. Hominin responses to Pleistocene environmental change in Arabia and South Asia, in: Head, M.J., Gibbard, P.L. (Eds.), Early-Middle Pleistocene Transitions: The Land-Ocean Evidence. Geological Society, London, pp. 305–319. https://doi.org/10.1144/GSL.SP.2005.247.01.18

Petraglia, M.D., Alsharekh, A.A., Breeze, P.S., Clarkson, C., Crassard, R., Drake, N.A., Groucutt, H.S., Jennings, R.P., Parker, A.G., Parton, A., Roberts, R.G., Shipton, C., Matheson, C., Al-Omari, A., Veall, M.A., 2012. Hominin Dispersal into the Nefud Desert and Middle Palaeolithic Settlement along the Jubbah Palaeolake, Northern Arabia. PLoS One 7. https://doi.org/10.1371/journal.pone.0049840

Pollastro, R.M., Karshbaum, A.S., Viger, R.J., 1999. Maps showing geology, oil and gas fields and geologic provinces of the Arabian Peninsula. U.S. Geol. Surv. Open-File Rep. 97-470-B 14. https://doi.org/https://doi.org/10.3133/ofr97470B

Pollastro, R.M., Persits, F.M., Steinshouer, D.W., 1997. Map showing geology, oil and gas fields, and geologic provinces of Iran. U.S. Geol. Surv. Open-File Rep. 97-470-G 10. https://doi.org/https://doi.org/10.3133/ofr97470G

Pourmand, A., Marcantonio, F., Schulz, H., 2004. Variations in productivity and eolian fluxes in the northeastern Arabian Sea during the past 110 ka. Earth Planet. Sci. Lett.

221, 39–54. https://doi.org/10.1016/S0012-821X(04)00109-8

Prospero, J.M., Ginoux, P., Torres, O., Nicholson, S.E., Gill, T.E., 2002. Environmental characterization of global sources of atmospheric soil dust identified with the Nimbus 7 Total Ozone Mapping Spectrometer (TOMS) absorbing aerosol product. Rev. Geophys. 40, 1–31. https://doi.org/10.1029/2000RG000095

Rashki, A., Kaskaoutis, D.G., Francois, P., Kosmopoulos, P.G., Legrand, M., 2015. Dust-storm dynamics over Sistan region, Iran : Seasonality, transport characteristics and affected areas. Aeolian Res. 16, 35–48. https://doi.org/10.1016/j.aeolia.2014.10.003

Reynolds, R.L., Reheis, M., Yount, J., Lamothe, P., 2006. Composition of aeolian dust in natural traps on isolated surfaces of the central Mojave Desert - Insights to mixing, sources, and nutrient inputs. J. Arid Environ. 66, 42–61. https://doi.org/10.1016/j.jaridenv.2005.06.031

Roberts, A.P., Rohling, E.J., Grant, K.M., Larrasoaña, J.C., Liu, Q., 2011. Atmospheric dust variability from Arabia and China over the last 500,000 years. Quat. Sci. Rev. 30, 3537–3541. https://doi.org/10.1016/j.quascirev.2011.09.007

Roberts, P., Stewart, M., Alagaili, A.N., Breeze, P.S., Candy, I., Drake, N.A., Groucutt, H.S., Scerri, E.M.L., Lee-Thorp, J., Louys, J., Zalmout, I.S., Al-Mufarreh, Y.S.A., Zech, J., Alsharekh, A.M., al Omari, A., Boivin, N., Petraglia, M.D., 2018. Fossil herbivore stable isotopes reveal middle Pleistocene hominin palaeoenvironment in 'Green Arabia.' Nat. Ecol. Evol. https://doi.org/10.1038/s41559-018-0698-9

Rosenberg, T.M., Preusser, F., Blechschmidt, I., Fleitmann, D., Jagher, R., Matter, A., 2012. Late Pleistocene palaeolake in the interior of Oman: A potential key area for the dispersal of anatomically modern humans out-of-Africa? J. Quat. Sci. 27, 13–16. https://doi.org/10.1002/jqs.1560

Rosenberg, T.M., Preusser, F., Fleitmann, D., Schwalb, A., Penkman, K., Schmid, T.W., Al-

Shanti, M.A., Kadi, K., Matter, A., 2011. Humid periods in southern Arabia: Windows of opportunity for modern human dispersal. Geology 39, 1115–1118. https://doi.org/10.1130/G32281.1

Rosenberg, T.M., Preusser, F., Risberg, J., Plikk, A., Kadi, K.A., Matter, A., Fleitmann, D., 2013. Middle and Late Pleistocene humid periods recorded in palaeolake deposits of the Nafud desert, Saudi Arabia. Quat. Sci. Rev. 70, 109–123. https://doi.org/10.1016/j.quascirev.2013.03.017

Saadat, S., Karimpour, M.H., Stern, C., 2010. Petrochemical Characteristics of Neogene and Quaternary Alkali Olivine Basalts from the Western Margin of the Lut Block , Eastern Iran 2, 87–106.

Sarr, A.C., Donnadieu, Y., Bolton, C.T., Ladant, J.B., Licht, A., Fluteau, F., Laugié, M., Tardif, D., Dupont-Nivet, G., 2022. Neogene South Asian monsoon rainfall and wind histories diverged due to topographic effects. Nat. Geosci. 15, 314–319. https://doi.org/10.1038/s41561-022-00919-0

Schepanski, K., 2018. Transport of mineral dust and its impact on climate. Geosci. 8. https://doi.org/10.3390/geosciences8050151

Schepanski, K., Tegen, I., Macke, A., 2012. Comparison of satellite based observations of Saharan dust source areas. Remote Sens. Environ. 123, 90–97. https://doi.org/10.1016/j.rse.2012.03.019

Scheuvens, D., Schütz, L., Kandler, K., Ebert, M., Weinbruch, S., 2013. Bulk composition of northern African dust and its source sediments - A compilation. Earth-Science Rev. 116, 170–194. https://doi.org/10.1016/j.earscirev.2012.08.005

Schnetger, B., Brumsack, H., Schale, H., Hinrichs, J., Dittert, L., 2000. Geochemical characteristics of deep-sea sediments from the Arabian Sea: a high-resolution study. Deep. Res. 47.

Sepulchre, P., Ramstein, G., Fluteau, F., Schuster, M., Tiercelin, J.J., Brunet, M., 2006. Tectonic Uplig and Eastern Africa Aridification. Science (80-.). 313, 1419–1423.

Sharifi, A., Murphy, L.N., Pourmand, A., Clement, A.C., Canuel, E.A., Naderi Beni, A., A.K. Lahijani, H., Delanghe, D., Ahmady-Birgani, H., 2018. Early-Holocene greening of the Afro-Asian dust belt changed sources of mineral dust in West Asia. Earth Planet. Sci. Lett. 481, 30–40. https://doi.org/10.1016/j.epsl.2017.10.001

Skonieczny, C., Bory, A., Bout-Roumazeilles, V., Abouchami, W., Galer, S.J.G., Crosta, X., Diallo, A., Ndiaye, T., 2013. A three-year time series of mineral dust deposits on the West African margin: Sedimentological and geochemical signatures and implications for interpretation of marine paleo-dust records. Earth Planet. Sci. Lett. 364, 145–156. https://doi.org/10.1016/j.epsl.2012.12.039

Skonieczny, C., McGee, D., Winckler, G., Bory, A., Bradtmiller, L.I., Kinsley, C.W., Polissar, P.J., De Pol-Holz, R., Rossignol, L., Malaizé, B., Polissar, P.J., Bradtmiller, L.I., Malaizé, B., Skonieczny, C., Kinsley, C.W., Bory, A., De Pol-Holz, R., Winckler, G., 2019. Monsoon-driven Saharan dust variability over the past 240,000 years. Sci. Adv. 5, eaav1887. https://doi.org/10.1126/sciadv.aav1887

Stern, R.J., Johnson, P., 2010. Continental lithosphere of the Arabian Plate: A geologic, petrologic, and geophysical synthesis. Earth-Science Rev. 101, 29–67. https://doi.org/10.1016/j.earscirev.2010.01.002

Stern, R.J., Kroner, A., 1993. Late Precambrian crustal evolution in NE Sudan: isotopic and geochronologic constraints. J. Geol. 101, 555–574. https://doi.org/10.1086/648249

Suresh, K., Singh, U., Kumar, A., Karri, D., Peketi, A., Ramaswamy, V., 2021. Provenance tracing of long-range transported dust over the Northeastern Arabian Sea during the southwest monsoon. Atmos. Res. 250, 105377. https://doi.org/10.1016/j.atmosres.2020.105377

Tam, W.W.S., Wong, T.W., Wong, A.H.S., Hui, D.S.C., 2012. Effect of dust storm events on daily emergency admissions for respiratory diseases. Respirology 17, 143–148. https://doi.org/10.1111/j.1440-1843.2011.02056.x

Tiedemann, R., Sarnthein, M., Shackleton, N., 1994. Astronomic timescale for the Pliocene Atlantic 180 dust flux records of Ocean Drilling Program site 659. Paleoceanography 9, 619–638.

Tierney, J.E., Lewis, S.C., Cook, B.I., LeGrande, A.N., Schmidt, G.A., 2011. Model, proxy and isotopic perspectives on the East African Humid Period. Earth Planet. Sci. Lett. 307, 103–112. https://doi.org/10.1016/j.epsl.2011.04.038

Torfstein, A., Goldstein, S.L., Stein, M., 2018. Enhanced Saharan dust input to the Levant during Heinrich stadials. Quat. Sci. Rev. 186, 142–155. https://doi.org/10.1016/j.quascirev.2018.01.018

Vaks, A., Bar-Matthews, M., Matthews, A., Ayalon, A., Frumkin, A., 2010. Middle-Late Quaternary paleoclimate of northern margins of the Saharan-Arabian Desert: Reconstruction from speleothems of Negev Desert, Israel. Quat. Sci. Rev. 29, 2647–2662. https://doi.org/10.1016/j.quascirev.2010.06.014

Vaks, A., Woodhead, J., Bar-Matthews, M., Ayalon, A., Cliff, R.A., Zilberman, T., Matthews, A., Frumkin, A., 2013. Pliocene-Pleistocene climate of the northern margin of Saharan-Arabian Desert recorded in speleothems from the Negev Desert, Israel. Earth Planet. Sci. Lett. 368, 88–100. https://doi.org/10.1016/j.epsl.2013.02.027

Van Hinsbergen, D.J.J., Buiter, S.J.H., Torsvik, T.H., Gaina, C., Webb, S.J., 2011. The formation and evolution of Africa from the Archaean to present: Introduction. Geol. Soc. Spec. Publ. 357, 1–8. https://doi.org/10.1144/SP357.1

Vance, D., Thirlwall, M., 2002. An assessment of mass discrimination in MC-ICPMS using Nd isotopes. Chem. Geol. 185, 227–240. https://doi.org/10.1016/S0009-2541(01)00402-

8

Washington, R., Todd, M., Middleton, N.J., Goudie, A.S., 2003. Dust-storm source areas determined by the total ozone monitoring spectrometer and surface observations. Ann. Assoc. Am. Geogr. 93, 297–313. https://doi.org/10.1111/1467-8306.9302003

Wurzler, S., Reisin, T.G., Levin, Z., 2000. Modification of mineral dust particles by cloud processing and subsequent effects on drop size distributions. J. Geophys. Res. Atmos. 105, 4501–4512. https://doi.org/10.1029/1999JD900980

Yobregat, E., Fitoussi, C., Bourdon, B., 2017. A new method for TIMS high precision analysis of Ba and Sr isotopes for cosmochemical studies. J. Anal. At. Spectrom. 32, 1388–1399. https://doi.org/10.1039/c7ja00012j

Yu, Y., Notaro, M., Kalashnikova, O. V., Garay, M.J., 2015. Climatology of summer Shamal wind in the Middle East. J. Geophys. Res. Atmos. 121, 40–49. https://doi.org/10.1002/2015JD023830.Received